

# Global millimeter VLBI array survey of ultracompact extragalactic radio sources at 86 GHz

Dhanya G. Nair<sup>1</sup>, Andrei P. Lobanov<sup>1,2</sup>, Thomas P. Krichbaum<sup>1</sup>, Eduardo Ros<sup>1</sup>, J. Anton Zensus<sup>1</sup>,  
Yuri Y. Kovalev<sup>3,4,1</sup>, Sang-Sung Lee<sup>5</sup>, Florent Mertens<sup>6</sup>, Yoshiaki Hagiwara<sup>7</sup>, Michael Bremer<sup>8</sup>,  
Michael Lindqvist<sup>9</sup>, and Pablo de Vicente<sup>10</sup>

<sup>1</sup> Max-Planck-Institut für Radioastronomie, Auf dem Hügel 69, 53121 Bonn, Germany

<sup>2</sup> Institut für Experimentalphysik, Universität Hamburg, Luruper Chaussee 149, 22761 Hamburg, Germany

<sup>3</sup> Astro Space Center of Lebedev Physical Institute, Profsoyuznaya 84/32, 117997 Moscow, Russia

<sup>4</sup> Moscow Institute of Physics and Technology, Dolgoprudny, Institutsky per., 9, Moscow region, 141700, Russia

<sup>5</sup> Korea Astronomy and Space Science Institute, Daedeokdae-ro 776, Yuseong-gu, Daejeon 34055, Republic of Korea

<sup>6</sup> SRON, Kapteyn Astronomical Institute, Landleven 12, 9747 AD Groningen, Netherlands

<sup>7</sup> 5-28-20 Hakusan, Bunkyo-ku, Natural Science Laboratory, Toyo University, Tokyo, Japan

<sup>8</sup> Institut de Radio Astronomie Millimétrique (IRAM), 300 rue de la Piscine, 38406 Saint Martin d'Hères, France

<sup>9</sup> Department of Space, Earth and Environment, Onsala Space Observatory, Sverige, Observatorievägen 90, Onsala, Sweden

<sup>10</sup> Observatorio Astronómico Nacional, Observatorio de Yebes, Cerro de la Palera S/N, 19141 Yebes, Spain

## ABSTRACT

**Context.** Very long baseline interferometry (VLBI) observations at 86 GHz (wavelength,  $\lambda = 3$  mm) reach a resolution of about 50  $\mu$ as, probing the collimation and acceleration regions of relativistic outflows in active galactic nuclei (AGN). The physical conditions in these regions can be studied by performing 86 GHz VLBI surveys of representative samples of compact extragalactic radio sources. **Aims.** To extend the statistical studies of compact extragalactic jets, a large global 86 GHz VLBI survey of 162 compact radio sources was conducted in 2010–2011 using the Global Millimeter VLBI Array (GMVA).

**Methods.** The survey observations were made in a snapshot mode, with up to five scans per target spread over a range of hour angles in order to optimize the visibility coverage. The survey data attained a typical baseline sensitivity of 0.1 Jy and a typical image sensitivity of 5 mJy/beam, providing successful detections and images for all of the survey targets. For 138 objects, the survey provides the first ever VLBI images made at 86 GHz. Gaussian model fitting of the visibility data was applied to represent the structure of the observed sources and to estimate the flux densities and sizes of distinct emitting regions (components) in their jets. These estimates were used for calculating the brightness temperature ( $T_b$ ) at the jet base (core) and in one or more moving regions (jet components) downstream from the core. These model-fit-based estimates of  $T_b$  were compared to the estimates of brightness temperature limits made directly from the visibility data, demonstrating a good agreement between the two methods.

**Results.** The apparent brightness temperature estimates for the jet cores in our sample range from  $2.5 \times 10^9$  K to  $1.3 \times 10^{12}$  K, with the mean value of  $1.8 \times 10^{11}$  K. The apparent brightness temperature estimates for the inner jet components in our sample range from  $7.0 \times 10^7$  K to  $4.0 \times 10^{11}$  K. A simple population model with a single intrinsic value of brightness temperature,  $T_0$ , is applied to reproduce the observed distribution. It yields  $T_0 = (3.77_{-0.14}^{+0.10}) \times 10^{11}$  K for the jet cores, implying that the inverse Compton losses dominate the emission. In the nearest jet components,  $T_0 = (1.42_{-0.19}^{+0.16}) \times 10^{11}$  K is found, which is slightly higher than the equipartition limit of  $\sim 5 \times 10^{10}$  K expected for these jet regions. For objects with sufficient structural detail detected, the adiabatic energy losses are shown to dominate the observed changes of brightness temperature along the jet.

**Key words.** galaxies: active – galaxies: jets – galaxies: quasars: general – radio continuum: galaxies – techniques: interferometric – surveys

## 1. Introduction

VLBI (Very long baseline interferometry) observations at 86 GHz (wavelength,  $\lambda = 3$  mm) enable detailed studies to be made of compact radio sources at a resolution of  $\sim (40 - 100)$   $\mu$ as. This resolution corresponds to linear scales as small as  $10^3 - 10^4$  Schwarzschild radii and uncovers the structure of the jet regions where acceleration and collimation of the flow takes place (Vlahakis & Königl 2004; Lee et al. 2008, 2016; Asada et al. 2014; Boccardi et al. 2016; Mertens et al. 2016).

To date, five 86 GHz VLBI surveys have been conducted (Beasley et al. 1997; Lonsdale et al. 1998; Rantakyrö et al. 1998; Lobanov et al. 2000; Lee et al. 2008, see Table 1), with the total number of objects imaged reaching just over a hun-

dred. No complete sample of objects imaged at 86 GHz has been established so far. Recent works (e.g., Homan et al. 2006; Cohen et al. 2007; Lister et al. 2016) have demonstrated that high-resolution studies of complete (or nearly complete) samples of compact jets yield a wealth of information about the intrinsic properties of compact extragalactic flows.

Measuring brightness temperature in a statistically viable sample enables the performance of detailed investigations of the physical conditions in this region. The distribution of observed brightness temperatures,  $T_b$ , derived at 86 GHz can be combined with the  $T_b$  distributions measured at lower frequencies (e.g., Kovalev et al. 2005). This can help to constrain the bulk Lorentz factor,  $\Gamma_j$ , and the intrinsic brightness temperature,  $T_0$ , of the jet plasma, using different types of population models of relativis-

tic jets (Vermeulen & Cohen 1994; Lobanov et al. 2000; Lister 2003; Homan et al. 2006). Changes of  $T_0$  in the compact jets with frequency can be used to distinguish between the emission coming from accelerating or decelerating plasma and from electron-positron or electron-proton plasma. Theoretical models predict  $T_0 \propto v^\epsilon$ , with  $\epsilon \approx 2.8$ , below a critical frequency  $v_{\text{break}}$  at which energy losses begin to dominate the emission (Marscher 1995). Above  $v_{\text{break}}$ ,  $\epsilon$  can vary from  $-1$  to  $+1$ , depending on the jet composition and dynamics. By measuring this break and the power-law slopes above and below, it would be possible to distinguish between different physical situations in the compact jets.

Previous studies (Lobanov et al. 2000; Lee et al. 2008) indicate that the value of  $v_{\text{break}}$  is likely to be below 86 GHz. Indeed, a compilation of brightness temperatures measured at 2, 8, 15, and 86 GHz (Lee et al. 2008) indicates that brightness temperatures measured at 86 GHz are systematically lower and  $v_{\text{break}}$  can be as low as 20 GHz. This needs to be confirmed on a complete sample observed at 86 GHz. If  $T_0$  starts to decrease at 86 GHz, there will be only a few sources suitable for VLBI  $> 230$  GHz and higher frequencies. Such a decrease of  $T_0$  will also provide a strong argument in favour of the decelerating jet model or particle-cascade models as discussed by Marscher (1995). In view of these arguments, it is important to undertake a dedicated 86 GHz VLBI study of a larger complete sample of extragalactic radio sources.

In this paper, we present results from a large global VLBI survey of compact radio sources carried out in 2010–2011 with the Global Millimeter VLBI Array (GMVA)<sup>1</sup>. This survey has provided images of 162 unique radio sources, increasing the total number of sources ever imaged with VLBI at 86 GHz by a factor of 1.5. The combined database resulting from this survey and Lee et al. (2008) comprises 256 sources. This information provides a basis for investigations of the collimation and acceleration of relativistic flows and probing the physical conditions in the vicinity of supermassive black holes.

The survey data reach a typical baseline sensitivity of 0.1 Jy and a typical image sensitivity of 5 mJy/beam. A total of 162 unique compact radio sources have been observed in this survey and all the sources are detected and imaged. With the present survey, the overall sample of compact radio sources imaged with VLBI at 86 GHz is representative down to  $\sim 0.5$  Jy for J2000 declinations of  $\delta \geq 15^\circ$ .

Section 2 describes the source selection and the survey observations. In Section 3, we describe the data processing, amplitude and phase calibration, imaging, model fitting procedures and a method for estimating errors of the model-fit parameters. Section 4 describes the images and derived parameters of the target sources. Examples of images of four selected sources obtained from the survey data are presented in Section 4.1 (the complete set of images of all of the target sources is presented in Appendix available electronically). Brightness temperatures of the survey sources are derived and discussed in Section 4.3. Section 5.1 describes population modelling of the brightness temperature distribution observed at the base (VLBI core) of the jet and in the innermost moving jet components. Evolution of the observed brightness temperature along the jet is studied in Section 5.2 for the target sources with sufficient extended emission detected.

## 2. GMVA survey of compact AGN

Dedicated VLBI observations at 86 GHz are made with the GMVA and with the Very Long Baseline Array (VLBA)<sup>2</sup> working in a stand-alone mode (VLBA also takes part in GMVA observations). The GMVA has been operating since 2002, superseding the operations of the Coordinated Millimeter VLBI Array (CMVA; Rogers et al. 1995) and earlier ad hoc arrangements employed since the early 1980s (Readhead et al. 1983). The GMVA carries out regular, coordinated observations at 86 GHz, providing good quality images with a typical angular resolution of  $\sim (50\text{--}70)\mu\text{as}$ .

The array comprises up to 16 telescopes located in Europe, the USA and Korea operating at a frequency of 86 GHz. The following telescopes took part in the GMVA observations for this survey in 2010 and 2011: eight VLBA antennae equipped with 3 mm receivers, the IRAM (Institut de Radio Astronomie Millimétrique) 30 m telescope on Pico Veleta (Spain), the phased six-element IRAM interferometer on Plateau de Bure (France), the MPIfR (Max-Planck-Institut für Radioastronomie) 100 m radio telescope in Effelsberg (Germany), the OSO (Onsala Space Observatory) 20 m radio telescope at Onsala (Sweden), the 14 m telescope in Metsähovi (Finland), and the OAN (Observatorio Astronómico Nacional) 40 m telescope in Yebes (Spain).

### 2.1. Source selection

The prime aims of the survey were to establish a complete sample of compact radio sources imaged with VLBI at 86 GHz and to study their morphology and polarization, to study the distribution of brightness temperatures, to investigate collimation and

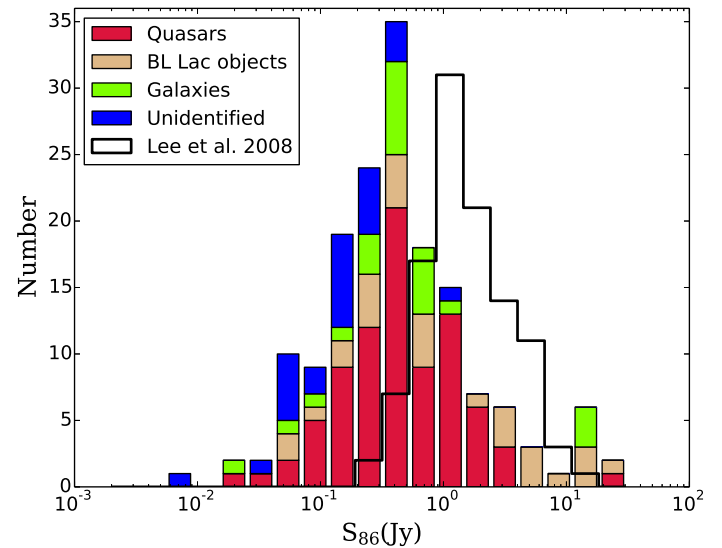


**Fig. 1.** Distribution of the total single dish flux density of the sources, measured at 86 GHz at Pico Veleta or Plateau de Bure during the observations,  $S_{86}$ , broken down according to different host galaxy types and compared to the respective distribution for the sources from the sample of Lee et al. (2008). The present survey provides a nearly twofold increase in the number of objects imaged with VLBI at 3 mm.

acceleration of relativistic flows and to probe physical conditions in the vicinity of supermassive black holes. To meet these aims, the survey target source list has been compiled from the MOJAVE (Monitoring of Jets in Active Galactic Nu-

<sup>1</sup> <http://www3.mpifr-bonn.mpg.de/div/vlbi/globalmm/>.

clei with VLBA Experiments) sample (Kellermann et al. 2004; Kovalev et al. 2005; Lister & Homan 2005; Lister et al. 2009), using the following selection criteria: *a*) 15 GHz correlated flux density,  $S_c \geq 0.5$  Jy on baselines of  $\geq 400$  M $\lambda$ ; *b*) compactness at longest spacings,  $S_c/S_{\text{VLBA}} \geq 0.4$  where  $S_{\text{VLBA}}$  is the 15 GHz total clean flux density; *c*) declination  $\delta \geq 15^\circ$ . With these selection criteria, a total of 162 unique sources have been selected, comprising 89 quasars, 26 BL Lac objects, 22 radio galaxies and 25 unidentified sources. Eight bright sources, 3C 84, OJ 287, 3C 273B, 3C 279, 3C 345, BL Lac, 0716+714 and 3C 454.3 have been added to this list for fringe finding and calibration purposes. The basic information about the selected target sources is summarized in Table 5.

The distribution of the total single dish flux of the sources, measured at 86 GHz at Pico Veleta or Plateau de Bure during the observations, is shown in Figure 1 and compared with the respective distribution of the source sample observed in Lee et al. (2008). This comparison shows that our survey observations probe objects at about one order of magnitude weaker sources and provide a roughly twofold increase of the total number of objects imaged with VLBI at 3 mm wavelength (see Table 5 for details).

## 2.2. Observations

The survey observations have been made over a total of six days (144 hours), scheduled within three separate GMVA sessions. Up to 14 telescopes took part in the observations (see Table 2). The observations were typically scheduled with five scans per hour, each of 300 seconds in duration. Gaps of five to ten minutes were introduced between the scans for antennae pointing at Effelsberg (Eb) and Pico Veleta (Pv) and for phasing of the Plateau de Bure (Pb) interferometer. This observing scheme yielded the total of 720 scans distributed between 174 observing targets (162 unique radio sources), ensuring that each object was observed with four to five scans distributed over a wide range of hour angles. Despite the rather modest observing time spent on each target, the large number of participating antennae ensured good *uv*-coverages for all survey sources down to the lowest declinations (see Figure 2).

The observations were performed at a sampling rate of 512 Mbit/sec and with a two-bit sampling. There were four intermediate frequencies (IFs) in Epoch A and C, and two IFs in Epoch B. The typical baseline sensitivities for a 20-second integration time are  $\approx 0.05$  Jy on the Pb–Pv baseline,  $\approx 0.1$  Jy on the Eb–Pv baseline,  $\approx 0.2$  Jy on the baselines between Eb/Pv and other antennae, and  $\approx 0.4$  Jy on the baselines between the VLBA antennae. With such baseline sensitivities and an on-source integration time of about 20 minutes, the typical point source sensitivity of a survey observation is  $\sim 5$  mJy/beam, which is sufficient to obtain robust images of most of the survey sources.

## 3. Data processing

### 3.1. Correlation and fringe fitting

The data were correlated at the DiFX correlator (Deller et al. 2011) of the Max-Planck-Institut für Radioastronomie (MPIfR) at Bonn. After correlation, the data were loaded into AIPS (Astronomical Image Processing System; Greisen 1990). After applying the correlator model, the residual fringe delays and rates were determined and corrected for both within the individual IFs (single-band fringe fitting) and between the IFs (multi-band fringe fitting).

At the first step of the fringe fitting, manual phaselcal correction was applied by obtaining the single band delay and delay rate solutions from a scan on a strong source that gives high signal-to-noise ratio (SNR) of the fringe solutions (an SNR  $\geq 7$  threshold was set) over the typical coherence time ( $\approx 20$  sec) for all the antennae. The resulting fringe solutions were applied to the entire dataset. After the manual phaselcal correction, antenna-based global fringe fitting (Schwab & Cotton 1983; Alef & Porcas 1986) was performed, setting the solution interval to the full scan length in order to improve the detection SNR. Pico Veleta was used as the reference antenna for almost all the data. Whenever Pico Veleta was not present in the data, Plateau de Bure or Pie Town were used as the reference antennae. To minimize the chance of false detections, the data were fringe fitted with a SNR threshold of five and a search window width of 200 nsec for the fringe delay and 400 mHz for the fringe rate.

Once the global fringe fit was done, the SNR of the fringe solutions were inspected for all the sources, and strong sources which give relatively very high SNR were determined. Whenever feasible, the solutions from those strong sources were interpolated to nearby weak sources, using a procedure similar to that adopted in the similar earlier VLBI survey observations at 86 GHz (cf., Lee et al. 2008). Application of the interpolated solutions has resulted in the detection of amplitude and phase signals for all of the survey targets.

### 3.2. Amplitude calibration

A priori amplitude calibration was done using the measured values of antenna gain and system temperature. The weather information from each station during the observation was used to correct for the atmospheric opacity. The initial opacity correction was implemented by setting the opacity  $\tau = 0.1$  and fitting for the receiver temperatures,  $T_{\text{rec}}$ . At the second step, the fitted receiver temperatures were used as initial values for fitting simultaneously for  $\tau$  and  $T_{\text{rec}}$ .

The accuracy and self-consistency of the amplitude calibration was checked with a procedure developed and used in the earlier 86 GHz survey experiments (Lobanov et al. 2000; Lee et al. 2008). The calibrated visibility data were model fitted for each of the survey targets, using two-dimensional Gaussian components and allowing for scaling the individual antenna gains by a constant factor. The resulting average gain scale corrections are listed in Table 4. The scale offsets are within 25 % for most of the antennae, except Metsähovi which had suffered from persistently bad weather during each of the three observing sessions. The averaged offsets are within about 3 % of the unity implying that there is no significant bias in the calibration and their r.m.s. (root mean square) is less than 10 % for each of the three observing epochs. Based on this analysis, we conclude that the a priori amplitude calibration should be accurate to within about 25 %, providing a sufficient initial calibration accuracy for the hybrid imaging of the source structure.

### 3.3. Hybrid imaging and model fitting

After the phase and amplitude calibration was applied on the data, the visibility data were averaged for 10 sec for most of the sources and in some cases, the data were averaged for 30 sec. The data were then processed in the the Caltech DIFMAP software package (Shepherd et al. 1994), modelling them with circular Gaussian patterns (model fitting; Fomalont 1999) and

**Table 1.** VLBI surveys at 86 GHz

Survey (1)	$N_{\text{ant}}$ (2)	$B_{\text{rec}}$ (3)	$\Delta S$ (4)	$\Delta I_m$ (5)	$D_{\text{img}}$ (6)	$N_{\text{obs}}$ (7)	$N_{\text{det}}$ (8)	$N_{\text{img}}$ (8)
Beasley et al. (1997)	3	112	$\sim 0.5$	...	...	51	12	...
Lonsdale et al. (1998)	2–5	112/224	$\sim 0.7$	...	...	79	14	...
Rantakyrö et al. (1998)	6–9	128	$\sim 0.5$	$\sim 30$	70	68	16	12
Lobanov et al. (2000)	3–5	224	$\sim 0.4$	$\sim 20$	100	28	26	14
Lee et al. (2008)	12	256	$\sim 0.3$	10	200	127	121	109
<i>This survey</i>	13–14	512	$\sim 0.1$	$\sim 5$	$> 400$	162	162	162

**Columns:** 1 – Survey ; 2 – number of participating antennae; 3 – recording bit rate [Mbps]; 4 – average baseline sensitivity [Jy]; 5 – average image sensitivity [mJy/beam]; 6 – typical dynamic range of images; 7 – number of sources observed; 8 – number of sources detected; 9 – number of sources imaged.

**Table 2.** Log of survey observations

Part (1)	Date (2)	$N_{\text{obj}}$ (3)	Pol. (4)	$w_{\text{bit}}$ (5)	BW (6)	$n_{\text{ch}}$ (7)	$n_{\text{bit}}$ (8)	Telescopes (9)
A	Oct 2010	68	LCP	512	128 (4IF x 32)	32	2	8 VLBA+(Eb,On,Mh,Pb,Pv)
B	May 2011	46	LCP	512	128 (2IF X 64)	64	2	8 VLBA+(Eb,On,Pb,Pv,Mh)
C	Oct 2011	60	LCP	512	128 (4IF x 32)	32	2	8 VLBA+(Eb,On,Pb,Pv,Mh,Ys)

**Columns:** 1 – survey epoch; 2 – observing date; 3 – number of objects observed; 4 – polarization; 5 – recording bit rate [Mbps]; 6 – total bandwidth (number of IF bands x IF bandwidth) [MHz]; 7 – number of frequency channels per IF band; 8 – correlator sampling [bits]; 9 – participating telescopes

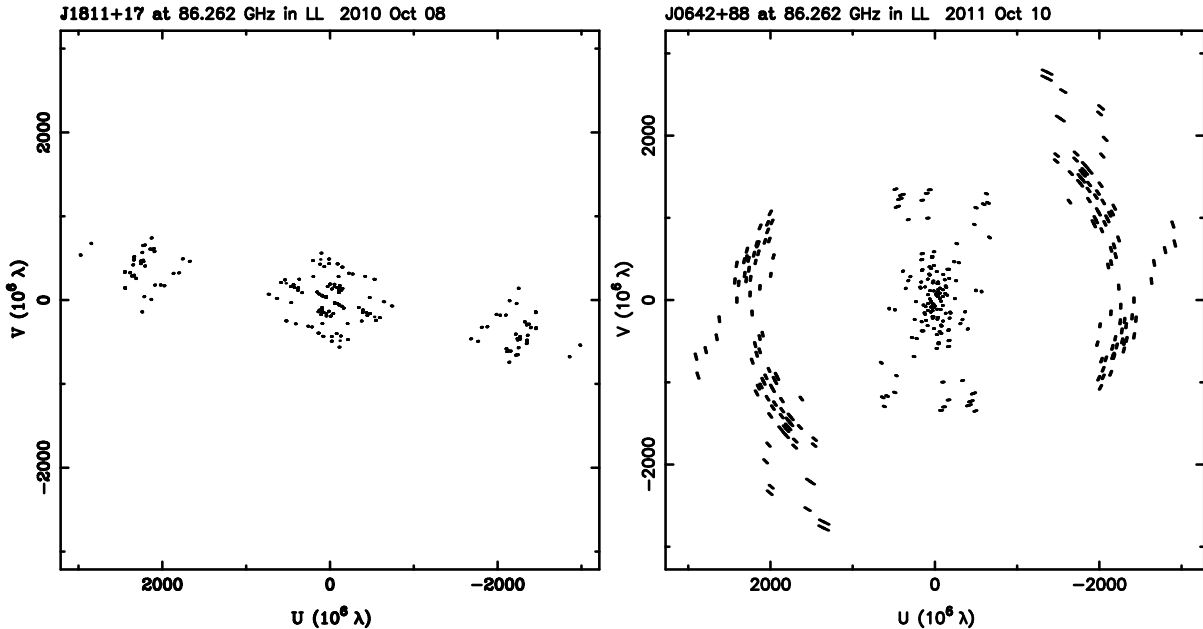


**Fig. 2.** Examples of  $uv$ -coverages of the survey observations for a low declination source (left; J1811+1704,  $\delta = +17^\circ$ ) and a high declination source (right; J0642+8811,  $\delta = +88^\circ$ ).

obtaining hybrid images. The data were not  $uv$ -tapered and the imaging was performed using the natural weighting.

The initial model fitting was performed on the calibrated data and was used, in some cases, to facilitate the hybrid imaging. The final model fitting was done on the self-calibrated data resulting from the hybrid imaging. The total number of Gaussian components used for model fitting a given source was determined using the  $\chi^2$  statistics of the fits. The final models were obtained when the addition of another Gaussian component did

not provide a statistically significant change of the  $\chi^2$  agreement factors (Schinzel et al. 2012).

The hybrid imaging procedure comprised the CLEAN deconvolution (Clark 1980) and self calibration (Cornwell & Fomalont 1999; Cornwell 1995). For most of the objects, the hybrid imaging procedure was initiated with a point source model. For objects with sparse visibility data, the initial Gaussian model fits were used as the initial models. Only visibility phases were allowed to be modified during the initial iterations of the hybrid imaging. At the last step, a single

**Table 3.** Participating telescopes

Name (1)	Code (2)	D [m] (3)	G [K/Jy] (4)	$T_{\text{sys}}$ [K] (5)	$\eta_A$ (6)	SEFD [Jy] (7)	$\Delta_{512,20}$ [mJy] (8)	$\sigma_{\text{rms}}$ [mJy] (9)
Brewster	Br	25	0.033	110	0.22	3333.3	23.44	164.09
Effelsberg	Eb	80 <sup>†</sup>	0.140	140	0.08	1000	12.84	89.87
Fort Davis	Fd	25	0.039	140	0.22	3589.7	24.32	170.28
Kitt Peak	Kp	25	0.028	100	0.22	3571.4	24.26	169.85
Los Alamos	La	25	0.042	120	0.22	2857.1	21.70	151.91
Metsähovi	Mh	14	0.017	300	0.3	17647.1	53.94	377.55
Mauna Kea	Mk	25	0.019	100	0.22	5263.2	29.45	206.18
North Liberty	Nl	25	0.022	130	0.22	5909.1	31.21	218.47
Onsala	On	20	0.049	250	0.43	5102	29.00	203.00
Owens Valley	Ov	25	0.035	120	0.22	3428.6	23.77	166.41
Plateau de Bure	Pb	36 <sup>‡</sup>	0.22	180	0.7	818.2	11.61	81.29
Pie Town	Pt	25	0.044	100	0.22	2272.7	19.36	135.52
Pico Veleta	Pv	30	0.153	100	0.6	653.6	...	...
Yebes	Ys	40	0.09	150	0.2	1666.7	16.58	116.03

**Columns:** 1 – telescope name; 2 – abbreviation for the telescope name; 3 – diameter; 4 – antenna gain; 5 – zenith system temperature; 6 – aperture efficiency; 7 – zenith SEFD; 8 – sensitivity on the baseline to Pico Veleta, for a 20 sec fringe fit interval and 512 Mbps recording rate; 9 – 7 $\sigma$  detection threshold. **Notes:** <sup>†</sup> – effective diameter at 86 GHz; <sup>‡</sup> – effective diameter in the phased array mode.

**Table 4.** Average antenna gain corrections

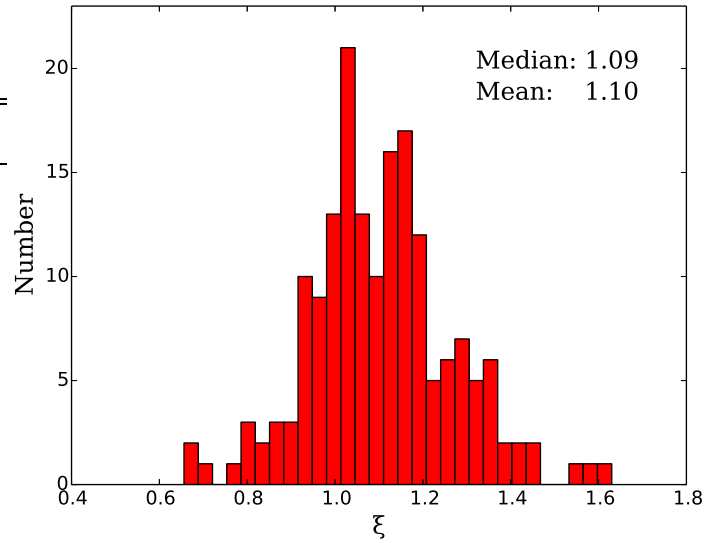
Telescope (1)	Epoch A (2)	Epoch B (3)	Epoch C (4)
Br	$1.008 \pm 0.406$	$1.054 \pm 0.137$	$1.010 \pm 0.192$
Eb	$1.103 \pm 0.264$	$1.028 \pm 0.224$	$0.925 \pm 0.182$
Fd	$0.992 \pm 0.206$	$1.105 \pm 0.289$	$0.958 \pm 0.162$
Kp	$0.881 \pm 0.154$	$0.933 \pm 0.104$	$0.931 \pm 0.102$
La	$0.819 \pm 0.199$	$0.940 \pm 0.172$	$0.987 \pm 0.133$
Mh	...	...	$1.620 \pm 0.573$
Mk	$0.919 \pm 0.256$	$1.188 \pm 0.438$	$0.844 \pm 0.199$
Nl	$1.224 \pm 0.386$	$1.190 \pm 0.296$	$0.798 \pm 0.264$
On	$0.934 \pm 0.292$	$0.935 \pm 0.114$	$0.889 \pm 0.147$
Ov	$0.900 \pm 0.371$	$0.868 \pm 0.148$	$0.939 \pm 0.382$
Pb	$1.081 \pm 0.146$	$1.087 \pm 0.225$	$1.095 \pm 0.203$
Pt	$0.841 \pm 0.113$	$0.878 \pm 0.109$	$1.041 \pm 0.098$
Pv	$1.006 \pm 0.116$	$1.088 \pm 0.220$	$1.010 \pm 0.086$
Ys	...	...	$1.009 \pm 0.196$
Array average	$1.037 \pm 0.084$	$0.991 \pm 0.074$	$1.027 \pm 0.097$

**Columns:** 1 – abbreviation for the participating telescope; 2,3,4 – average and r.m.s of antenna gains for observing epochs A, B, and C, respectively.

time constant antenna gain correction factor was applied to the visibility amplitudes (hence not allowing for time variable antenna gains in order to avoid the imprint of model errors into data). The parameters of the final images are listed in Table 6, together with the correlated flux densities measured on short and long baselines.

The quality of the residual noise in the final images, which ideally should have a zero-mean Gaussian distribution, was checked by calculating the expectation value for the maximum absolute flux density  $|S_{r,\text{exp}}|$  in a residual image (Lee et al. 2008),

$$|S_{r,\text{exp}}| = \sigma_r \sqrt{2} \ln \left( \frac{N_{\text{pix}}}{\sqrt{2\pi}\sigma_r} \right)^{\frac{1}{2}}, \quad (1)$$

**Fig. 3.** Distribution of the noise quality factor  $\xi_r$  for the residual images of all the sources in the survey.

where  $N_{\text{pix}}$  is the total number of pixels in the image. The quality of the residual noise is given by  $\xi_r = S_r/S_{r,\text{exp}}$ , where  $S_r$  is the maximum flux density in the residual image and  $\sigma_r$  is the r.m.s noise in the residual image. When the residual noise approaches Gaussian noise,  $\xi_r$  tends to 1. If  $\xi_r > 1$ , not all the structure has been adequately recovered; if  $\xi_r < 1$ , the image model has an excessively large number of degrees of freedom (Lobanov et al. 2006). Figure 3 shows the overall distribution of  $\xi_r$  for the residual maps of all the sources in this survey. Column 14 in Table 6 shows the quality factor,  $\xi_r$  obtained for all the 3 mm images implying that the images adequately represent the source structure detected in the visibility data. The Gaussianity of the residual noise is also reflected in the median and the mean of the  $\xi_r$  distributions, which are within 10 % of the unity factor.

In order to check the effect of the amplitude (antenna gain) corrections applied during the final self calibration step, we com-

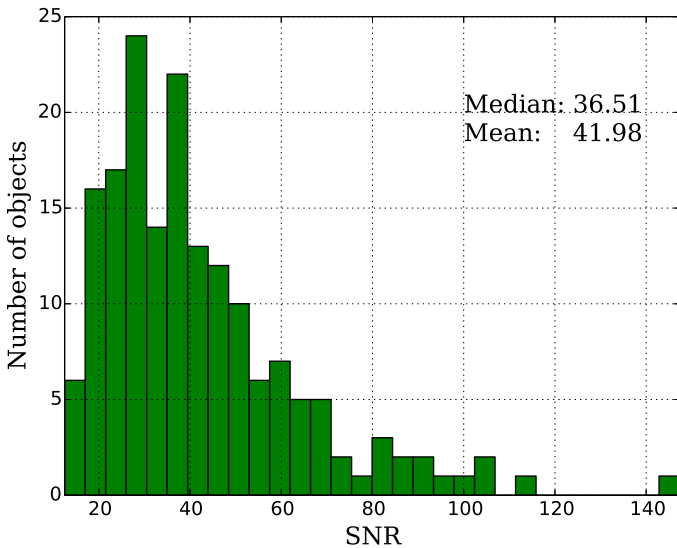


**Fig. 4.** Distribution of the imaging signal-to-noise ratios (SNR) of all the sources in the survey calculated from the ratio of the peak flux density of the map,  $S_p$ , to the r.m.s noise in the map,  $\sigma_{\text{rms}}$ .

pared the visibility amplitudes obtained without and with it. This was done by comparing the ratios of the visibility amplitudes obtained without and with the antenna gain correction on short  $B_S$  and long  $B_L$  baselines (see Table 6). The average of the ratios are found to be  $(1.24 \pm 0.18)$  and  $(1.01 \pm 0.14)$  for the short and long baselines, respectively. These ratios imply that the amplitude self-calibration did not introduce substantial gain corrections, thus further indicating the overall good quality of the a priori amplitude calibration of the survey data.

#### 3.4. Gaussian models of the source structure

The final self calibrated data were fitted with circular Gaussian components, using the initial model fits as a starting guess. The resulting models were used to obtain the total,  $S_{\text{tot}}$ , and peak flux density,  $S_{\text{peak}}$ , the size,  $d$ , and the positional offset, (in polar coordinates  $r, \theta$ ) of the component from the brightest region (core) at the base of the jet, taken to be at the coordinate origin. The uncertainties of the model parameters were estimated analytically, based on the SNR of detection of individual components, following (Fomalont 1999) and (Schinzel et al. 2012):

$$\begin{aligned} \sigma_{\text{peak}} &= \sigma_{\text{rms}} \left( 1 + \frac{S_{\text{peak}}}{\sigma_{\text{rms}}} \right)^{1/2}, \quad \sigma_{\text{tot}} = \sigma_{\text{peak}} \left( 1 + \frac{S_{\text{tot}}^2}{S_{\text{peak}}^2} \right)^{1/2}, \\ \sigma_d &= d \frac{\sigma_{\text{peak}}}{S_{\text{peak}}}, \quad \sigma_r = \frac{1}{2} \sigma_d, \quad \sigma_\theta = \tan \left( \frac{\sigma_r}{r} \right), \end{aligned} \quad (2)$$

where  $\sigma_{\text{rms}}$  is the r.m.s. noise in the residual image after subtraction of the Gaussian model fit. To assess whether a given component is extended (resolved), the minimum resolvable size of the component was also calculated and compared with the size obtained with the model fitting. The minimum resolvable size,  $d_{\min}$  of a Gaussian component is given in Lobanov (2005) as

$$d_{\min} = \frac{2^{(1+\beta/2)}}{\pi} \left[ \pi a b \log \left( \frac{\text{SNR} + 1}{\text{SNR}} \right) \right]^{1/2}, \quad (3)$$

where  $a$  and  $b$  are the axes of the restoring beam, SNR is the signal-to-noise ratio, and  $\beta$  is the weighing function that is 0 for

natural weighting or 2 for uniform weighting. For components that have size estimates  $< d_{\min}$ , the latter is taken as an upper limit of the size and used for estimating the uncertainties of the other model fit parameters of the respective component (see Table 7).

#### 3.5. Brightness temperature estimates

We use the total flux density  $S_{\text{tot}}$  and size  $d$  of the model fit components to estimate the brightness temperature,  $T_b = I_v c^2 / 2k_B \nu$  (with  $\nu$ ,  $k_B$ , and  $c$  denoting the observing frequency, the Boltzmann constant, and the light speed, respectively) of the individual emitting regions in the jets.

For a circular Gaussian component,  $I_v = (4 \log 2/2) S_{\text{tot}} / d^2$ , and the respective brightness temperature can be obtained from

$$T_b [\text{K}] = 1.22 \times 10^{12} \left( \frac{S_{\text{tot}}}{\text{Jy}} \right) \left( \frac{d}{\text{mas}} \right)^{-2} \left( \frac{\nu}{\text{GHz}} \right)^{-2} (1+z). \quad (4)$$

The factor  $(1+z)$  reflects the effect of the cosmological redshift  $z$  on the observed brightness temperature. For the sources with unknown redshift, we calculated the brightness temperature simply in the observer's frame of reference. If the size of the Gaussian component  $d$  is less than  $d_{\min}$ , given by Equation (3), the latter is used for estimating the lower limit on  $T_b$ .

In addition to this estimate, we also use visibility-based estimates of brightness temperature (Lobanov 2015) and calculate the minimum brightness temperature,

$$T_{b,\min} [\text{K}] = 3.09 \left( \frac{V_q}{\text{mJy}} \right) \left( \frac{B_L}{\text{km}} \right)^2, \quad (5)$$

and limiting resolved brightness temperature,

$$T_{b,\lim} [\text{K}] = 1.14 \left( \frac{V_q + \sigma_q}{\text{mJy}} \right) \left( \frac{B_L}{\text{km}} \right)^2 \left( \ln \frac{V_q + \sigma_q}{V_q} \right)^{-1}, \quad (6)$$

directly from the visibility amplitude,  $V_q$ , and its error,  $\sigma_q$ , measured at a given long baseline,  $B_L$ , in the survey data.

### 4. Results

#### 4.1. Images

Using the procedures described above, we have made hybrid maps of all 174 observations of 162 unique sources in this survey. For 138 objects, the survey provides the first ever VLBI images made at 86 GHz. Most of the imaged sources show extended radio emission, revealing the jet morphology down to sub-parsec scales. For a small number of weaker sources with poor  $uv$ -coverages, only the brightest core at the base of the jet could be imaged. To illustrate our results, we present images of four weak target radio sources J1130+3815, J0700+1709, J1044+8054 and J0748+2400 in Figure 6 (the complete figure featuring the full set of images obtained from this survey is presented in Appendix available electronically).

Figure 5 illustrates the properties of the survey sample by plotting the distributions of the correlated flux density,  $S_L$ , measured on long baselines and the total flux density,  $S_{\text{CLEAN}}$ , in the CLEAN images of the observed sources. Both distributions indicate that objects with flux densities  $\gtrsim 80$  mJy can be successfully detected and imaged with the survey data, signifying the sensitivity improvement by a factor of approximately two compared to the observations presented in Lee et al. (2008). The mean of the correlated flux density at the longest baseline,  $S_L$ , is 0.2 Jy.

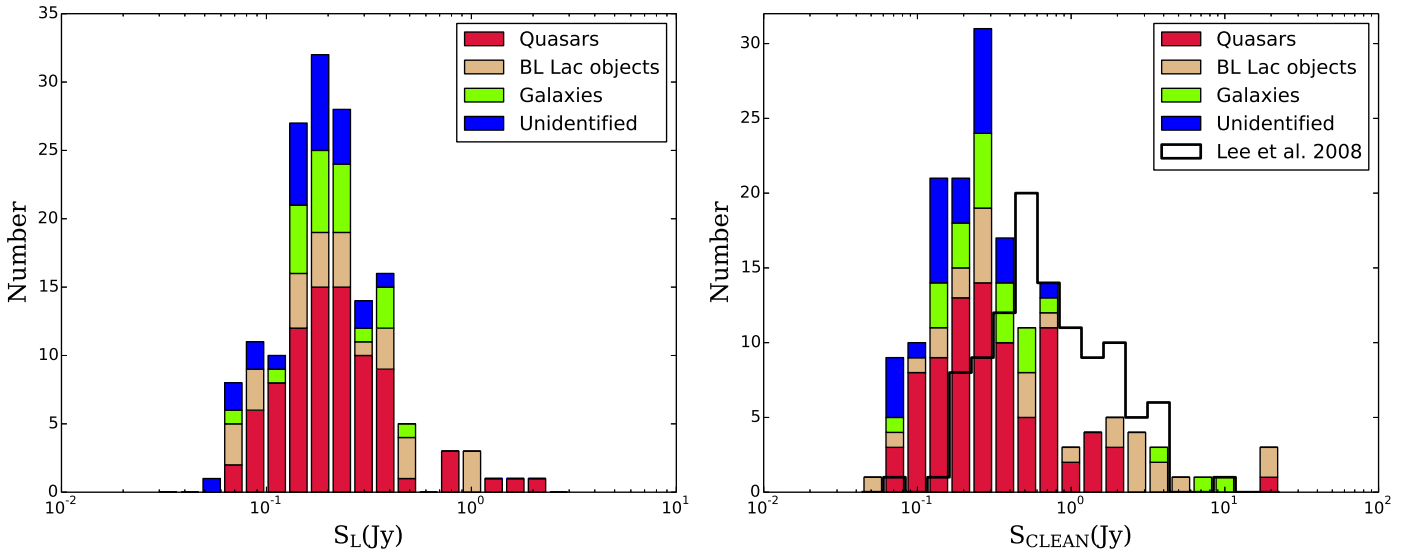


**Fig. 5.** Distribution of the correlated flux densities corresponding to the longest baselines,  $S_L$  (left) and the total clean image flux density,  $S_{\text{CLEAN}}$  of the survey targets broken down according to different host galaxy types (right). The distribution of  $S_{\text{CLEAN}}$  for the sources in this survey is also compared with the respective distribution for the sources from the sample of Lee et al. (2008) on the right panel.

Amongst 157 sources whose  $S_L$  can be measured at projected baselines longer than  $2000 M\lambda$ , 135 sources have an  $S_L$  greater than 0.1 Jy.

In Table 6, we present the basic parameters of the images, listing (1) source name, (2) observing epoch, (3) single dish 86 GHz flux density,  $S_{86}$ , measured at Pico Veleta or Plateau de Bure, (4) correlated flux density on the shortest baseline,  $S_S$ , (5) shortest baseline,  $B_S$ , (6) correlated flux density on the longest baseline,  $S_L$ , (7) longest baseline,  $B_L$ , (8) major axis,  $B_a$ , (9) minor axis,  $B_b$ , and (10) position angle,  $B_{\text{PA}}$  of the major axis of the restoring beam, (11) total CLEAN flux density,  $S_{\text{tot}}$ , and (12) peak flux density,  $S_{\text{peak}}$ , in the image, (13) image r.m.s noise,  $\sigma_{\text{rms}}$ , and (14) the quality factor of the residual noise in the image,  $\xi_r$ .

Table 7 summarizes the model fits obtained for all of the survey sources providing (1) the source name, (2) observing epoch, (3) sequential number of the Gaussian component, (4) total flux density,  $S_t$ , and (5) peak flux density,  $S_{\text{peak}}$ , of the component, (6) size,  $d$ , of the component, (7) separation,  $r$ , and (8) position angle,  $\theta$  of the component with respect to the brightest feature in the model (core, taken to be located at the coordinate origin), (9) brightness temperature,  $T_{b,\text{mod}}$ , estimated from the model fit, and (10) minimum,  $T_{b,\text{min}}$  and (11) limiting resolved,  $T_{b,\text{lim}}$ , brightness temperatures estimated from the visibility amplitudes (Lobanov 2015) at the longest baselines given in Column 7 in Table 6.

Table 7 contains the model fit parameters for a total 174 VLBI cores and 205 jet components, with 42 and 37 of these unresolved, as reflected also in the lower limits of the model-fit-based brightness temperature estimates,  $T_{b,\text{mod}}$ , listed for these components.

#### 4.2. Source compactness

Compactness of the source structure can be evaluated by comparing the single dish flux density,  $S_{86}$ , listed in Table 6, to the total clean flux density,  $S_{\text{CLEAN}}$ , listed in Table 6 and the core flux density,  $S_{\text{CORE}}$ , listed in Table 7, to the total clean flux density,  $S_{\text{CLEAN}}$ . These comparisons are presented in Figure 7.

To study the relation between the total and VLBI flux densities, we apply the Pearson correlation test. The Pearson correlation coefficient calculated for  $S_{86}$  and  $S_{\text{CLEAN}}$  gives a significant value of 0.924 for this survey and 0.908 for this survey combined with the results from Lee et al. (2008). The respective plot in the left panel of Figure 7 indicates that almost all the flux measured by a single dish (here Pv or PdB) is recovered in the VLBI clean flux. The median of the core dominance index defined as  $S_{\text{CORE}}/S_{\text{CLEAN}}$  is 0.84, and the two are also correlated, as demonstrated in the right panel of Figure 7.

Figure 7 shows that the stronger sources have more structures (right panel) some of which are completely resolved out even on the shortest baselines of the survey observations (left panel). A small number of cases for which  $S_{\text{CLEAN}} > S_{86}$  or  $S_{\text{CORE}} > S_{\text{CLEAN}}$  are observed for the weaker objects. These can be reconciled with the errors in the measurements, and they essentially imply very compact objects, with  $S_{86} \approx S_{\text{CLEAN}}$  and  $S_{\text{CORE}} \approx S_{\text{CLEAN}}$ , respectively.

#### 4.3. Brightness temperatures

In our further analysis, we use the model-fit-based and visibility-based estimates of the brightness temperature of the VLBI bright core (base) and the inner ( $r_{\text{proj}} < 1 \text{ pc}$ ) jet components, taking into account the resolution limits of the data at 3 mm. The brightness temperature estimates for the jet cores in our sample range from  $2.5 \times 10^9 \text{ K}$  to  $1.3 \times 10^{12} \text{ K}$ . The brightness temperature estimates for the inner jet components in our sample range from  $7.0 \times 10^7 \text{ K}$  to  $4.0 \times 10^{11} \text{ K}$ . The median and mean of the brightness temperature distribution for the core regions are  $8.6 \times 10^{10} \text{ K}$  and  $1.8 \times 10^{11} \text{ K}$ , respectively. For the inner jet components, the respective figures are  $7.2 \times 10^9 \text{ K}$  and  $2.2 \times 10^{10} \text{ K}$ . This shows that the brightness temperature drops by approximately an order of magnitude already on sub-parsec scales in the jets, with inverse Compton, synchrotron, and adiabatic losses subsequently dominating the energy losses (cf. Marscher 1995; Lobanov & Zensus 1999). Only 8 % of the jet cores show a brightness temperature greater than  $5 \times 10^{11} \text{ K}$  and only 3 % have a brightness temperature greater than  $10^{12} \text{ K}$ .

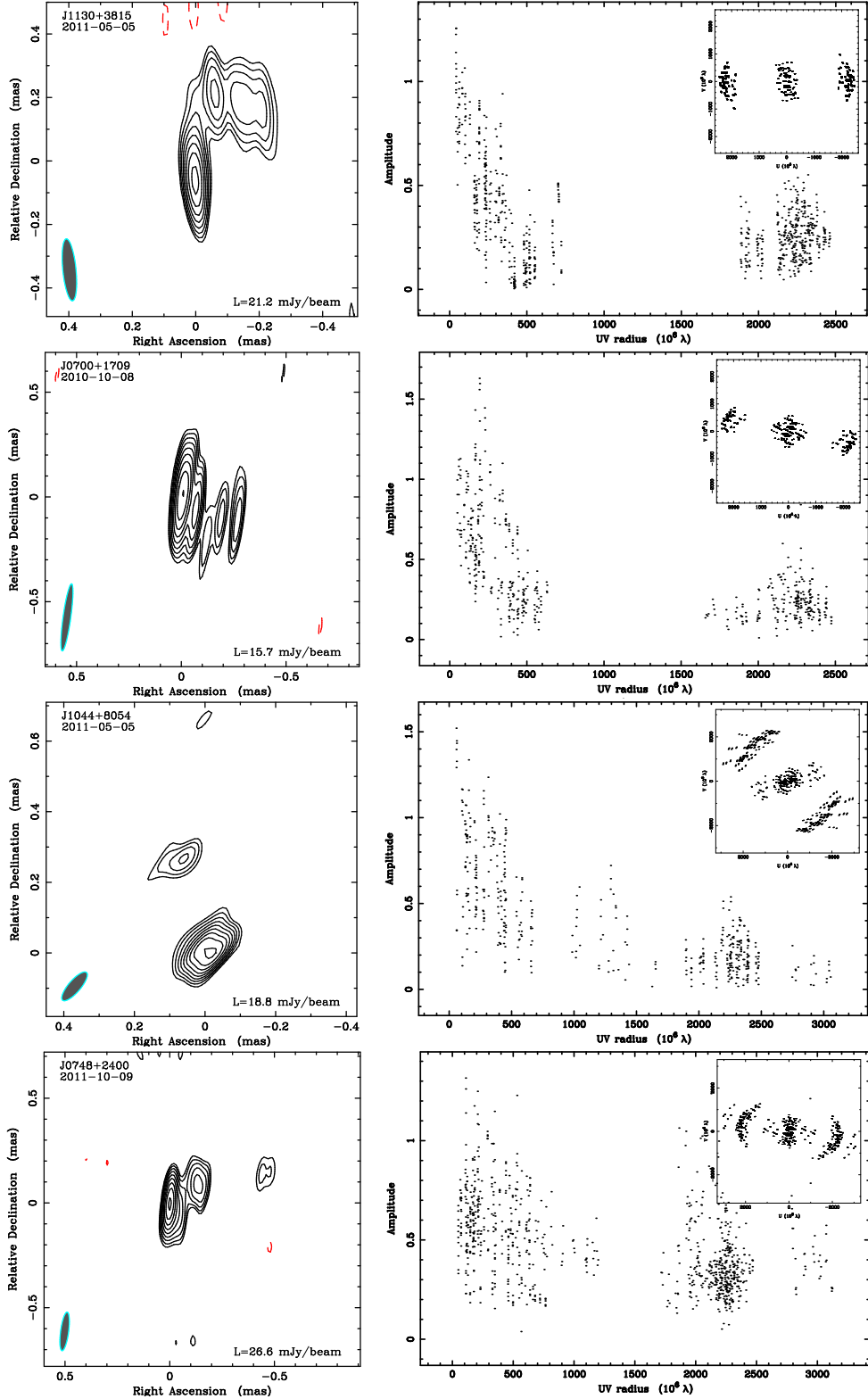


**Fig. 6.** GMVA maps of J1130+3815, J0700+1709, J1044+8054, and J0748+2400 (left panel), shown together with the respective radial amplitude distributions (right panel) and *uv*-coverages (inset in the right panel) of the respective visibility datasets. The contouring of images is made at  $3\sigma_{\text{rms}} \times (-1, \sqrt{2}, 2, \dots)$  levels, with  $\sigma_{\text{rms}}$  representing the off-source r.m.s noise in the residual image. The lowest contour in the maps, L = 21.2 mJy/beam, 15.8 mJy/beam, 18.8 mJy/beam, and 26.6 mJy/beam, respectively. A total of 174 contour maps of 162 unique sources at 3 mm in this survey are available in the online journal.

We also inspect the distribution of the minimum and maximum limiting brightness temperature of the core components (using averaged values of brightness temperature for objects with multiple observations) in the sample, making these esti-

mates from the visibility amplitudes on the longest baselines (Lobanov 2015). The minimum,  $T_{\text{b},\text{min}}$ , and limiting,  $T_{\text{b},\text{lim}}$ , brightness temperatures are given in Table 7, in columns 10 and 11, respectively.

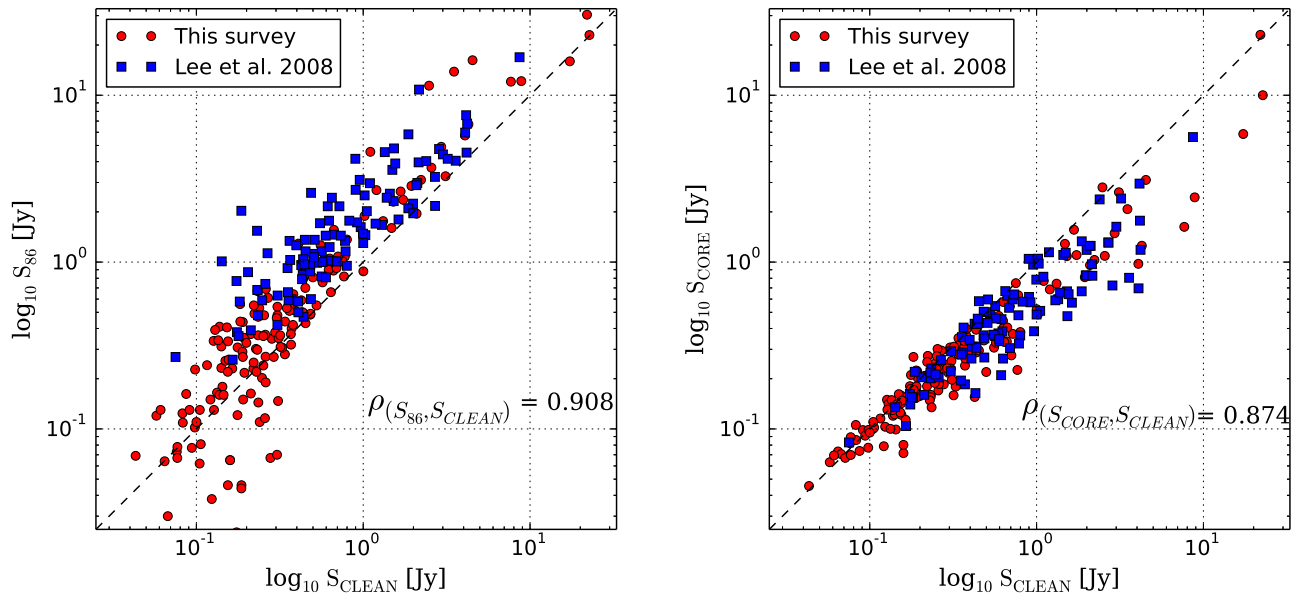


**Fig. 7.** Compactness parameters,  $S_{86}/S_{\text{CLEAN}}$  and  $S_{\text{core}}/S_{\text{CLEAN}}$  are shown on the left and right panel respectively, where  $S_{86}$  is the single dish 86 GHz flux density measured at Pico Veleta or Plateau de Bure. The Pearson correlation coefficients  $\rho(S_{86}, S_{\text{CLEAN}}) = 0.908$  and  $\rho(S_{\text{CORE}}, S_{\text{CLEAN}}) = 0.874$  are obtained for the combined data from this survey and Lee et al. (2008).

The median and mean of the maximum limiting brightness temperature distribution for the core regions is  $1.06 \times 10^{11}$  K and  $3.0 \times 10^{11}$  K, respectively. We find that the limiting  $T_{b,\text{lim}}$  correlates well with  $T_{b,\text{mod}}$  estimated from imaging method as seen in Figure 8, supporting the fidelity of  $T_{b,\text{mod}}$  measurements obtained from model fitting. The residual logarithmic distribution of the  $T_{b,\text{mod}}/T_{b,\text{lim}}$  ratio is well approximated by the Gaussian PDF, with mean value,  $\mu = 0.001$  and standard deviation,  $\sigma = 0.46$ .

## 5. Discussion

### 5.1. Modelling the observed brightness temperatures

The brightness temperature distribution can be used for obtaining estimates of the conditions in the extra galactic radio sources and to test the models proposed for the inner jets (Marscher 1995; Lobanov et al. 2000; Homan et al. 2006; Lee et al. 2008). A basic population model (Lobanov et al. 2000) can be used for representing the observed brightness temperature distribution under the assumption that the jets have the same intrinsic brightness temperature,  $T_0$ , Lorentz factor,  $\Gamma_j$ , and synchrotron spectral index,  $\alpha$  ( $S_\nu \propto \nu^\alpha$ ), and they are randomly oriented in space (within the limits of viewing angles,  $\theta$ , required by Doppler boosting bias). The jets are also assumed to remain straight within the spatial scales ( $\sim 0.5 - 10$  pc) probed by the observations.

The assumptions of single values of  $T_0$  and  $\Gamma_j$  describing the whole sample are clearly simplified, as jets are known to feature a range of Lorentz factors (see Lister et al. 2016, and references therein). However, as has been shown earlier (Lobanov et al. 2000), factoring a distribution of Lorentz factors into the present model is not viable without amending the brightness temperature measurements with additional information, preferably about the apparent speeds of the target sources. We are currently compiling such a combined database, and will engage in a more de-

tailed modelling of the compact jets after the completion of this database.

In a population of jets described by the settings summarized above, the measured brightness temperature,  $T_b$ , is determined solely by the relativistic Doppler boosting of the jet emission. Therefore, the observed brightness temperature,  $T_b$ , can be related to the intrinsic brightness temperature,  $T_0$ , so that  $T_b = T_0 \delta^{1/\epsilon}$ , where the power index  $\epsilon$  is  $1/(2 - \alpha)$  for a continuous jet (steady state jet) and  $1/(3 - \alpha)$  for a jet with spherical blobs (or optically thin “plasmoids”), and  $\delta$  is the Doppler factor.

The probability of finding a radio source with the brightness temperature  $T_b$  in such a population of sources is

$$p(T_b) \propto \left[ \frac{2 \Gamma_j (T_b/T_0)^\epsilon - (T_b/T_0)^{2\epsilon} - 1}{\Gamma_j^2 - 1} \right]^{\frac{1}{2}}. \quad (7)$$

The lower end of the observed distribution of brightness temperatures depends on the sensitivity of VLBI data since the flux of the observed sample is biased by Doppler boosting (Lobanov et al. 2000). The lowest brightness temperature that can be measured from our data,  $T_{b,\text{sens}}$ , can be obtained from

$$T_{b,\text{sens}}[\text{K}] = 1.65 \times 10^5 \left( \frac{\sigma_{\text{rms}}}{\text{mJy/beam}} \right) \left( \frac{b}{\text{mas}} \right)^{-2}, \quad (8)$$

where  $\sigma_{\text{rms}}$  is the array sensitivity in mJy/beam and  $b$  is the average size of the resolving beam. In this survey, the typical observation time on a target source  $\Delta t$  is 20 minutes and bandwidth is 128 MHz. Therefore, the value of beam size for the sources in this survey is 0.12 mas and the  $\sigma_{\text{rms}}$  of the array is 0.54 mJy/beam. Thus, we have obtained a  $3\sigma$  level estimation of  $T_{b,\text{sens}}$  as  $2.0 \times 10^8$  K using Equation 8, which is set as the lowest brightness temperature in modelling.

We normalize the results obtained from Equation (7) to the number of objects in the lowest bin of the histogram. For our modelling, we first make a generic assumption of  $\alpha = -0.7$  (homogeneous synchrotron source) and use  $\Gamma_j \approx 10$  implied

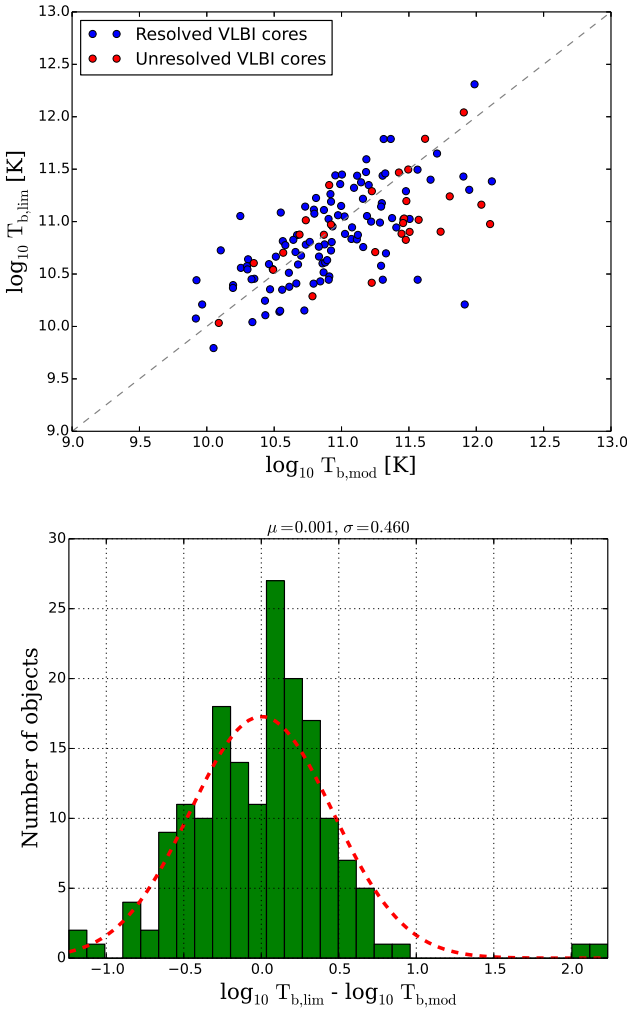


**Fig. 8.** Comparison of  $T_{b,mod}$  measured from circular Gaussian representation of source structure and  $T_{b,lim}$  estimated from the interferometric visibilities at  $uv$ -radii within 10% of the maximum baseline  $B_{max}$  in the data for a given source (top panel). Correlation between the two distributions is illustrated by the residual logarithmic distribution of the  $T_{b,mod}/T_{b,limit}$  ratio (bottom panel), which is well approximated by the Gaussian distribution with  $\mu = 0.001$  and  $\sigma = 0.46$ .

from the kinematic analysis of the MOJAVE VLBI survey data (Lister et al. 2016). We assume that the jet is continuous, so  $\epsilon = 0.37$  is taken. For the population modelling analysis, we have included the data from Lobanov et al. (2000), Lee et al. (2008), and the present survey, yielding a final database of 271 VLBI core components and 344 jet components. For objects with multiple measurements, we have used the median of the measurements. The resulting model distributions obtained for various values of  $T_0$  are shown in Figures (9–10) for the VLBI cores and the inner jet components, respectively.

This approach yields  $T_{0,core} = (3.77^{+0.10}_{-0.14}) \times 10^{11}$  K for the VLBI cores and  $T_{0,jet} = (1.42^{+0.16}_{-0.19}) \times 10^{11}$  K for the inner jet components. The estimated  $T_{0,core}$  is in good agreement with the inverse Compton limit of  $\approx 5.0 \times 10^{11}$  K (Kellermann & Pauliny-Toth 1969), beyond which the inverse Compton effect causes rapid electron energy losses and extinguishes the synchrotron radiation. The inferred  $T_{0,jet}$  of jet components are about a factor of three higher than the equipartition limit of  $\approx 5 \times 10^{10}$  K (Readhead et al. 1983) for which the magnetic field energy and particle energy are in equilibrium. This may indicate that opacity is still non-negligible in these regions

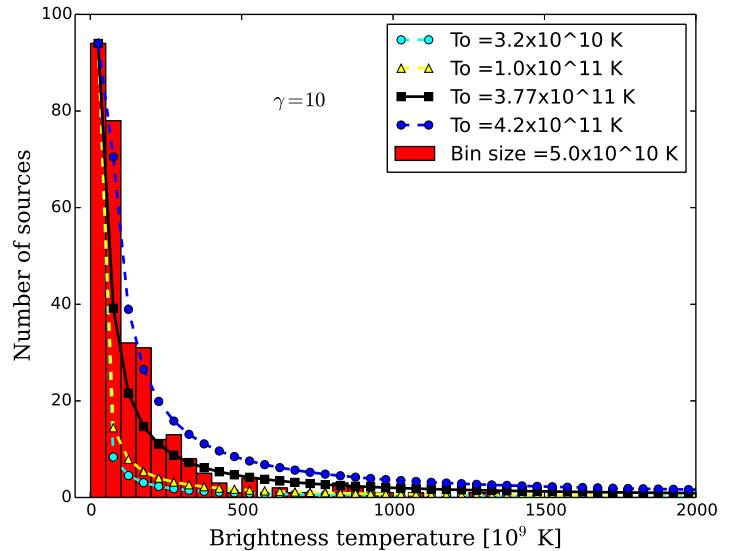


**Fig. 9.** Distribution of the brightness temperatures,  $T_b$ , measured in the core components and represented by the population models calculated for  $\Gamma_j = 10$  and different values of  $T_0$ . The best approximation of the observed  $T_b$  distribution is obtained with  $T_{0,core} = (3.77^{+0.10}_{-0.14}) \times 10^{11}$  K. For better viewing of the observed distribution, one core component with a very high  $T_b = 5.5 \times 10^{12}$  K for the source BL Lac obtained from Lee et al. (2008) is not shown but is included in the modelling.

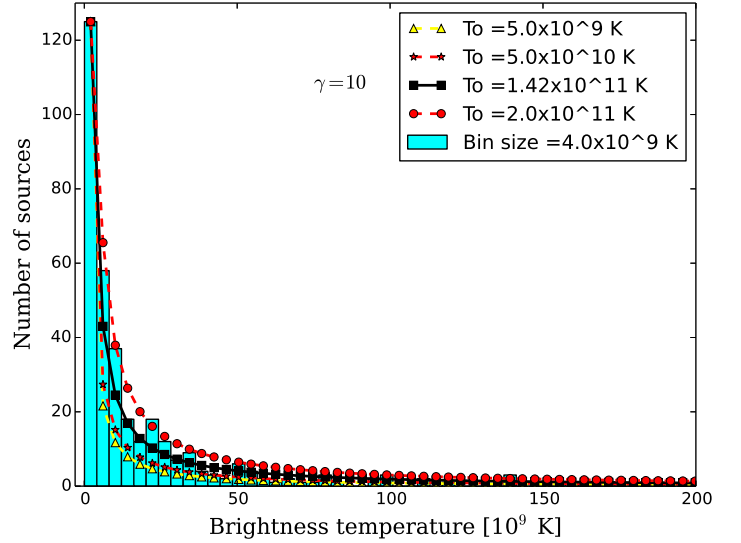


**Fig. 10.** Distribution of the brightness temperatures,  $T_b$ , measured in the inner jet components and represented by the population models calculated for  $\Gamma_j = 10$  and different values of  $T_0$ . The best approximation of the observed  $T_b$  distribution is obtained with  $T_{0,jet} = (1.42^{+0.16}_{-0.19}) \times 10^{11}$  K.

of the flow. The intrinsic brightness temperature obtained for the cores is within the upper limit  $5.0 \times 10^{11}$  K predicted for the population modelling of the cores (Lobanov et al. 2000).

A simultaneous fit for  $T_0$  and  $\Gamma_j$  is impeded by the implicit correlation,  $T_0 \propto \Gamma_j^a$  (with  $a \approx 2-3$ ), between these two parameters, as implied by Equation (7). This is also illustrated in Figure 11, from which a dependence  $T_0[\text{K}] \approx (7.7 \times 10^8) \Gamma_j^{2.7}$  can be inferred for the fit to the brightness temperatures measured in the VLBI cores. This correlation between  $T_0$  and  $\Gamma_j$  precludes simultaneously fitting for both these parameters, and hence the

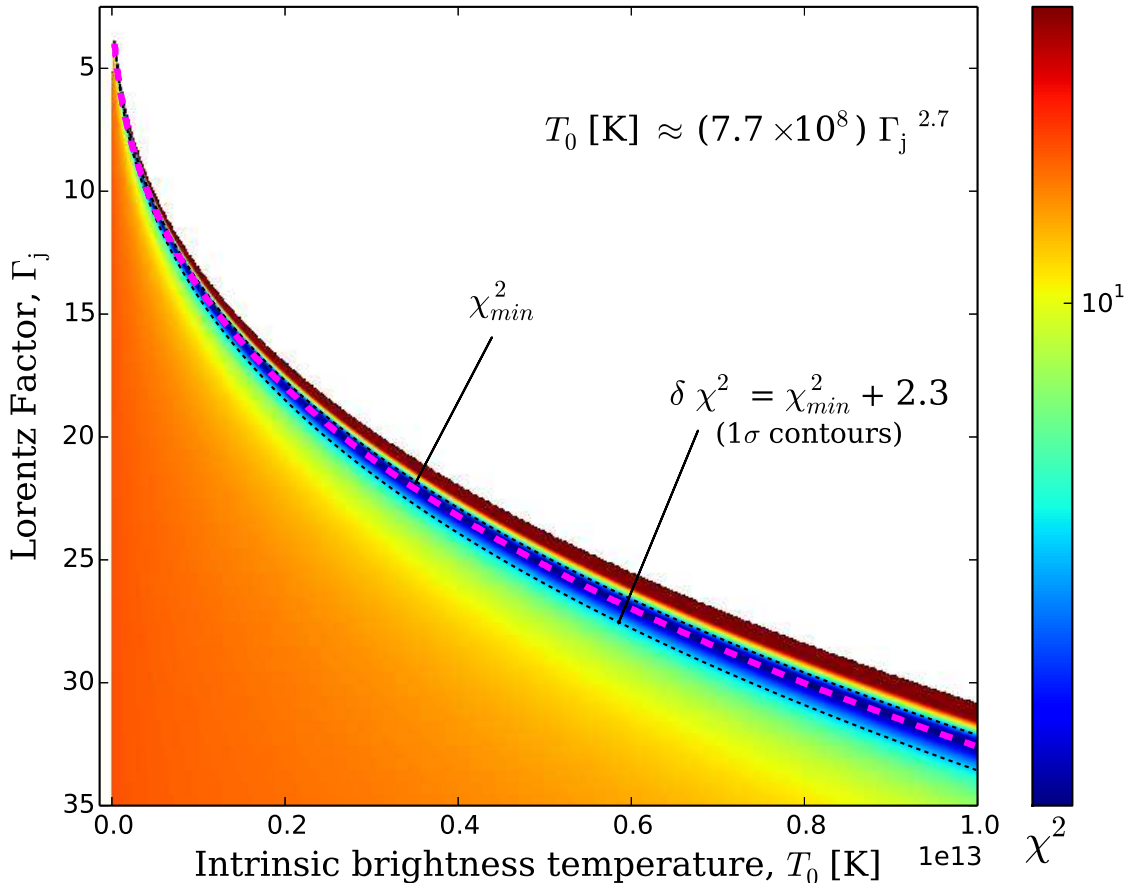


**Fig. 11.** Two-dimensional  $\chi^2$  distribution plot in the  $\Gamma_j - T_0$  space, calculated for the brightness temperatures measured in the VLBI cores. The blank area shows the ranges of the parameter space disallowed by the observed distribution. The distribution of the  $\chi^2$  values indicates a  $(\Gamma_j - T_0)$  correlation, with  $T_0[\text{K}] \approx (7.7 \times 10^8) \Gamma_j^{2.7}$ , thus precluding a simultaneous fit for  $\Gamma_j$  and  $T_0$ .

Lorentz factor has to be constrained (or assumed) separately. One should also keep in mind that this correlation results from the model description and does not have an immediate physical implication. Equation (7) clearly shows that the predicted distribution of  $T_b$  is valid within the range

$$(\Gamma_j - \sqrt{\Gamma_j^2 - 1}) \leq \left(\frac{T_0}{T_b}\right)^\epsilon \leq (\Gamma_j + \sqrt{\Gamma_j^2 - 1}). \quad (9)$$

The region outside this range is represented by the blank area in Figure 11.

The intrinsic brightness temperature we obtained is higher than the mean and median observed brightness temperature  $T_b$ . This is readily explained by the Doppler deboosting. For a given viewing angle,  $\theta$ , sources with  $\Gamma_j > 1/\theta$  would be deboosted so that the observed brightness temperature will be reduced below its intrinsic value. It can be easily shown that the observed and intrinsic brightness temperatures are equal if the jet viewing angle is given by

$$\theta_{\text{eq}} = \arccos \left[ \frac{1 - (1/\Gamma_j) (T_0/T_b)^\epsilon}{\sqrt{1 - \Gamma_j^{-2}}} \right]. \quad (10)$$

For the VLBI cores, the mean of the observed  $T_b$  is  $1.8 \times 10^{11}$  K and intrinsic  $T_{0,\text{core}}$  is  $3.77 \times 10^{11}$  K, therefore, the resulting  $\theta_{\text{eq}} =$

$29^\circ$  for  $\Gamma_j = 10$  and  $\epsilon = 0.37$ . In this case any object observed at a larger viewing angle would be deboosted resulting in a lower observed  $T_b$  than intrinsic  $T_0$ .

## 5.2. Testing the adiabatic expansion of jets

As discussed in Sections 4.3 and 5.1, intrinsic  $T_0$  and the observed  $T_b$  in core and jets show that the brightness temperature drops by approximately a factor of two to ten already on sub-parsec scales in the jets. This evolution might occur with the inverse Compton, synchrotron, and adiabatic losses subsequently dominating the energy losses (cf., Marscher 1995; Lobanov & Zensus 1999).

For four objects in our data (3C84, 0716+714, 3C454.3, and J2322+507) for which multiple jet components have been identified during the model fitting, it is possible to use the brightness temperatures of the jet components to test whether the evolution of the jet brightness on sub parsec scales could be explained by adiabatic energy losses (Marscher & Gear 1985). For this analysis, we assume that the jet components are independent relativistic shocks embedded in the jet plasma, which has a power-law distribution  $N(E) dE \propto E^{-s} dE$ , where  $s$  is the energy spectral index that depends on spectral index  $\alpha$  as  $\alpha = (1 - s)/2$ , and is pervaded by the magnetic field  $B \propto d^{-a}$ , where  $d$  is the width of the jet and  $a$  depends on the type of magnetic field ( $a = 1$  for poloidal magnetic field and 2 for toroidal magnetic field). With

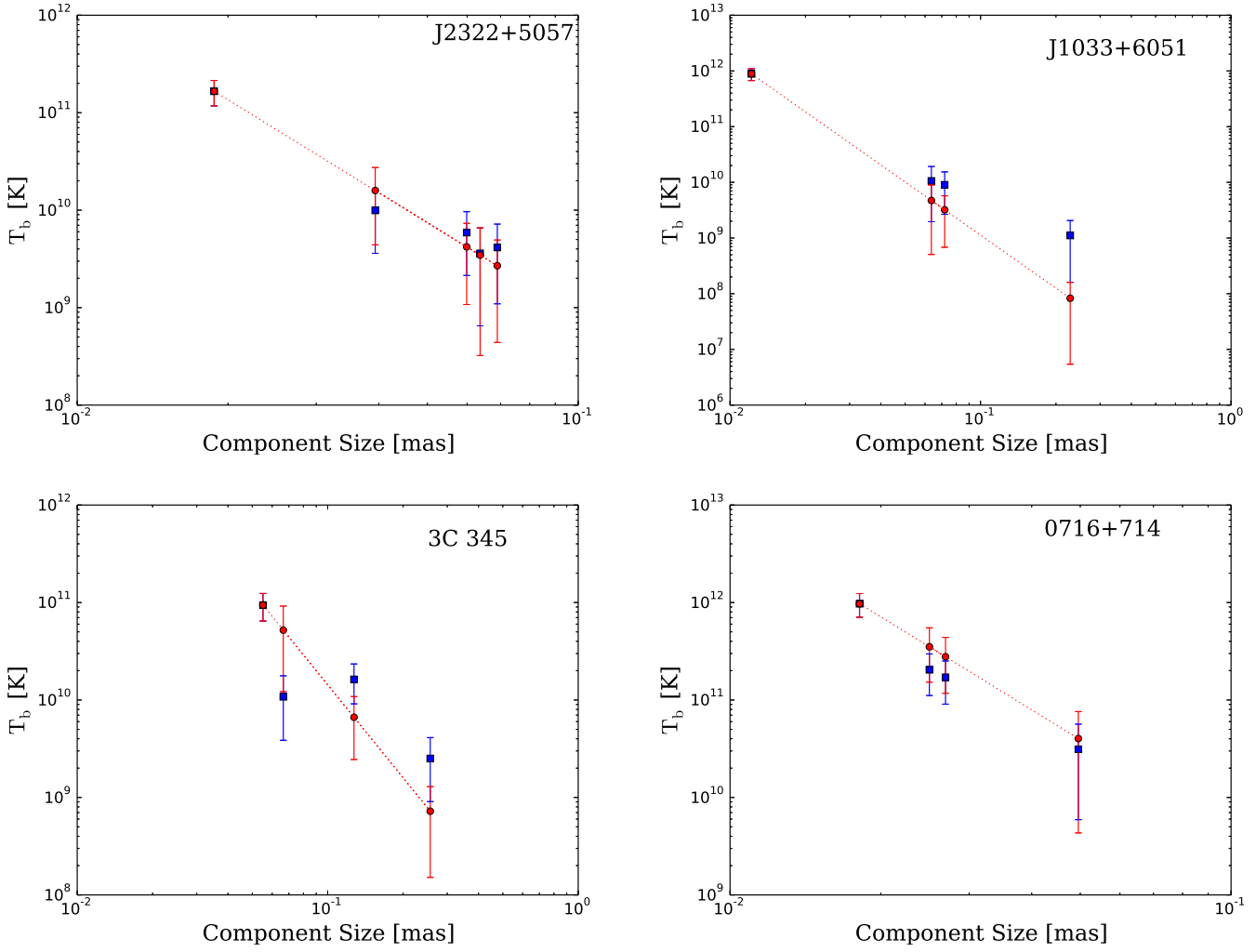


**Fig. 12.** Changes of the brightness temperature as a function of jet width for four sources – J2322+5037, J1033+6051, 3C 345, and 0716+714 from this survey. Blue squares denote the measured  $T_b$  from this survey. The red circles connected with a dotted line represent theoretically expected  $T_b$  under the assumption of adiabatic jet expansion. The initial brightness temperature in each jet is assumed to be the same as that measured in the VLBI core.

these assumptions, we can relate the brightness temperatures,  $T_{b,J}$ , of the jet components to the brightness temperature,  $T_{b,C}$ , of the core (Lobanov et al. 2000; Lee et al. 2008),

$$T_{b,J} = T_{b,C} \left( \frac{d_J}{d_C} \right)^{-\xi}, \quad (11)$$

where  $d_J$  and  $d_C$  are the measured sizes of the jet component and core, respectively, and

$$\xi = \frac{2(2s + 1) + 3a(s + 1)}{6}. \quad (12)$$

Assuming the synchrotron emission with spectral index  $\alpha = -0.5$ , we use  $s = 2.0$  and adopt  $a = 1.0$  for the description of the magnetic field in the jet. With these assumptions, we calculate the predicted  $T_{b,J}$  for individual jet components and compare them in Figure 12 to the measured brightness temperatures. The measured and predicted values of brightness temperature agree well, and this suggests that the jet components can be viewed as adiabatically expanding relativistic shocks (cf., Kadler et al. 2004; Pushkarev & Kovalev 2012; Kravchenko et al. 2016).

## 6. Summary

We have used the Global Millimeter VLBI Array (GMVA) to conduct a large global 86 GHz VLBI survey comprising 174 snapshot observations of 162 unique targets selected from a sample of compact radio sources. The survey observations have reached a typical baseline sensitivity of 0.1 Jy and a typical image sensitivity of 5 mJy/beam, owing to the increased recording bandwidth of the GMVA observations and the participation of very sensitive European antennae at Pico Veleta and Plateau de Bure. All of the 162 objects have been detected and imaged, thereby increasing the total number of AGN imaged with VLBI at 86 GHz by a factor of  $\sim 1.5$ . We imaged 138 sources for the first time with VLBI at 86 GHz through this survey.

We have used Gaussian model fitting to represent the structure of the observed sources and estimate the flux densities and sizes of the core and jet components. We used the model fit parameters and visibility data on the longest baselines to make independent estimates of brightness temperatures at the jet base as described by the most compact and bright “VLBI core” component. These estimates are consistent with each other. For sources with extended structure detected, the model fit parameters have been also used to calculate brightness temperature in the jet com-

ponents downstream from the core. The apparent brightness temperature estimates for the jet cores in our sample range from  $2.5 \times 10^9$  K to  $1.3 \times 10^{12}$  K, with the mean value of  $1.8 \times 10^{11}$  K. The brightness temperature estimates for the inner jet components in our sample range from  $7.0 \times 10^7$  K to  $4.0 \times 10^{11}$  K. The overall amplitude calibration error for the observations is about 25%.

We describe the observed brightness temperature distributions by a basic population model which assumes that all jets are intrinsically similar and can be described by a single value of the intrinsic brightness temperature,  $T_0$ , and Lorentz factor,  $\Gamma_j$ . The population modelling shows that our data are consistent with a population of sources that has  $T_0 = (3.77^{+0.10}_{-0.14}) \times 10^{11}$  K in the VLBI cores and  $T_0 = (1.42^{+0.16}_{-0.19}) \times 10^{11}$  K in the jets, both obtained for  $\Gamma_j = 10$  adopted from the kinematic analysis of the MOJAVE VLBI survey of AGN jets (Lister et al. 2016). A correlation between  $T_0$  and  $\Gamma_j$  inherent to the model description precludes fitting for these two parameters simultaneously. We find that a relation  $T_0[\text{K}] \approx (7.7 \times 10^8) \Gamma_j^{2.7}$  is implied for this modelling framework by the survey data. For sources with sufficient structural detail, there is an agreement between the brightness temperatures measured in multiple components along the jet and the predicted brightness temperatures for relativistic shocks with adiabatic losses dominating the emission.

The results of the survey can be combined with brightness temperature measurements made from VLBI observations at lower frequencies (e.g., Kovalev et al. 2005; Petrov et al. 2007) to study the evolution of  $T_0$  with frequency and along the jet (Lee et al. 2008, 2016). This approach can be used to better constrain the bulk Lorentz factor and the intrinsic brightness temperature, to distinguish between the acceleration and deceleration scenario for the flow (cf., Marscher 1995), and to test several alternative acceleration scenarios including hydrodynamic acceleration (Bodo et al. 1985), acceleration by tangled magnetic field (Heinz & Begelman 2000), and magnetohydrodynamics acceleration (Vlahakis & Königl 2004).

## Acknowledgments

We thank the staff of the observatories participating in the GMVA, the MPIfR Effelsberg 100 m telescope, the IRAM Plateau de Bure Interferometer, the IRAM Pico Veleta 30 m telescope, the Metsähovi Radio Observatory, the Onsala Space Observatory, and the VLBA. The VLBA is an instrument of the National Radio Astronomy Observatory, which is a facility of the National Science Foundation operated under cooperative agreement by Associated Universities, Inc. This research has made use of the NASA/IPAC Extragalactic Database (NED) which is operated by the Jet Propulsion Laboratory, California Institute of Technology, under contract with the National Aeronautics and Space Administration. This research has made use of the SIMBAD database, operated at CDS, Strasbourg, France and also the Sloan Digital Sky Survey (SDSS).

Dhanya G. Nair is a member of the International Max Planck Research School (IMPRS) for Astronomy and Astrophysics at the Universities of Bonn and Cologne. Thanks to Biagina Boccardi, Jun Liu, Laura Vega García, Jae-Young Kim, Ioannis Myserlis, Vassilis Karamanavis, Jeff Hodgson, Shoko Koyama, Bindu Rani and Karl M. Menten for their valuable suggestions and support in this research. The author also thanks Walter Alef and Alessandra Bertarini for helping in the correlation of the 86 GHz VLBI data used in this research. Thanks to Uwe Bach and Salvador Sánchez who have helped in the observation and calibration at Effelsberg radio telescope and IRAM Pico Veleta radio telescope, respectively. Sang-Sung Lee was supported by the National Research Foundation of Korea (NRF) grant funded by the Korea government (MSIP) (No. NRF-2016R1C1B2006697). Yuri Y. Kovalev was supported in part by the government of the Russian Federation (agree-

ment 05.Y09.21.0018) and by the Alexander von Humboldt Foundation.

## References

- Alef, W. & Porcas, R. W. 1986, A&A, 168, 365
- Asada, K., Nakamura, M., Doi, A., Nagai, H., & Inoue, M. 2014, ApJ, 781, L2
- Beasley, A. J., Dhawan, V., Doeleman, S., & Phillips, R. B. 1997, in Millimeter-VLBI Science Workshop, ed. R. Barvainis & R. B. Phillips, 53
- Boccardi, B., Krichbaum, T. P., Bach, U., Bremer, M., & Zensus, J. A. 2016, A&A, 588, L9
- Bodo, G., Ferrari, A., Massaglia, S., & Tsinganos, K. 1985, A&A, 149, 246
- Clark, B. G. 1980, A&A, 89, 377
- Cohen, M. H., Lister, M. L., Homan, D. C., et al. 2007, ApJ, 658, 232
- Cornwell, T. 1995, in Astronomical Society of the Pacific Conference Series, Vol. 82, Very Long Baseline Interferometry and the VLBA, ed. J. A. Zensus, P. J. Diamond, & P. J. Napier, 39
- Cornwell, T. & Fomalont, E. B. 1999, in Astronomical Society of the Pacific Conference Series, Vol. 180, Synthesis Imaging in Radio Astronomy II, ed. G. B. Taylor, C. L. Carilli, & R. A. Perley, 187
- Deller, A. T., Brisken, W. F., Phillips, C. J., et al. 2011, PASP, 123, 275
- Fomalont, E. B. 1999, in Astronomical Society of the Pacific Conference Series, Vol. 180, Synthesis Imaging in Radio Astronomy II, ed. G. B. Taylor, C. L. Carilli, & R. A. Perley, 301
- Greisen, E. W. 1990, in Acquisition, Processing and Archiving of Astronomical Images, ed. G. Longo & G. Sedmak, 125–142
- Heinz, S. & Begelman, M. C. 2000, ApJ, 535, 104
- Homan, D. C., Kovalev, Y. Y., Lister, M. L., et al. 2006, ApJ, 642, L115
- Kadler, M., Ros, E., Lobanov, A. P., Falcke, H., & Zensus, J. A. 2004, A&A, 426, 481
- Kellermann, K. I., Lister, M. L., Homan, D. C., et al. 2004, ApJ, 609, 539
- Kellermann, K. I. & Pauliny-Toth, I. I. K. 1969, ApJ, 155, L71
- Kovalev, Y. Y., Kellermann, K. I., Lister, M. L., et al. 2005, AJ, 130, 2473
- Kravchenko, E. V., Kovalev, Y. Y., Hovatta, T., & Ramakrishnan, V. 2016, MNRAS, 462, 2747
- Lee, S.-S., Lobanov, A. P., Krichbaum, T. P., et al. 2008, AJ, 136, 159
- Lee, S.-S., Lobanov, A. P., Krichbaum, T. P., & Zensus, J. A. 2016, ApJ, 826, 135
- Lister, M. L. 2003, ApJ, 599, 105
- Lister, M. L., Aller, M. F., Aller, H. D., et al. 2016, AJ, 152, 12
- Lister, M. L., Cohen, M. H., Homan, D. C., et al. 2009, AJ, 138, 1874
- Lister, M. L. & Homan, D. C. 2005, AJ, 130, 1389
- Lobanov, A. P. 2005, arXiv:astro-ph/0503225
- Lobanov, A. P. 2015, A&A, 574, A84
- Lobanov, A. P., Krichbaum, T. P., Graham, D. A., et al. 2000, A&A, 364, 391
- Lobanov, A. P., Krichbaum, T. P., Witzel, A., & Zensus, J. A. 2006, PASJ, 58, 253
- Lobanov, A. P. & Zensus, J. A. 1999, ApJ, 521, 509
- Lonsdale, C. J., Doeleman, S. S., & Phillips, R. B. 1998, AJ, 116, 8
- Marscher, A. P. 1995, Proceedings of the National Academy of Science, 92, 11439
- Marscher, A. P. & Gear, W. K. 1985, ApJ, 298, 114
- Mertens, F., Lobanov, A. P., Walker, R. C., & Hardee, P. E. 2016, A&A, 595, A54
- Petrov, L., Hirota, T., Honma, M., et al. 2007, AJ, 133, 2487
- Pushkarev, A. B. & Kovalev, Y. Y. 2012, A&A, 544, A34
- Rantakyrö, F. T., Baath, L. B., Backer, D. C., et al. 1998, A&AS, 131, 451
- Readhead, A. C. S., Mason, C. R., Mofett, A. T., et al. 1983, Nature, 303, 504
- Rogers, A. E. E., Phillips, R. B., & Lonsdale, C. J. 1995, in Bulletin of the American Astronomical Society, Vol. 27, American Astronomical Society Meeting Abstracts, 1300
- Schinzel, F. K., Lobanov, A. P., Taylor, G. B., et al. 2012, A&A, 537, A70
- Schwab, F. R. & Cotton, W. D. 1983, AJ, 88, 688
- Shepherd, M. C., Pearson, T. J., & Taylor, G. B. 1994, in BAAS, Vol. 26, Bulletin of the American Astronomical Society, 987–989
- Vermeulen, R. C. & Cohen, M. H. 1994, ApJ, 430, 467
- Vlahakis, N. & Königl, A. 2004, ApJ, 605, 656
- Wenger, M., Ochsenbein, F., Egret, D., et al. 2000, A&AS, 143, 9

**Table 5.** List of Sources

Source (J2000) (1)	Source (B1950) (2)	Common Name (3)	Epoch (4)	$\alpha_{2000}$ (5)	$\delta_{2000}$ (6)	$z$ (7)	Type (8)	$m_v$ (9)
J0013+4051	0010+405	4C 40.01	C	00 13 31.130201	+40 51 37.14403	0.2560	G	17.9
J0017+8135	0014+813		B	00 17 08.474904	+81 35 08.13656	3.3660	Q	16.5
J0030+7037	0027+703		B	00 30 14.412959	+70 37 40.06069	...	U	17.0
J0034+2754	0032+276		C	00 34 43.486179	+27 54 25.72112	2.9642	G	18.0
J0044+6803	0041+677		B	00 44 50.759603	+68 03 02.68574	...	U	...
J0046+2456	0043+246		A	00 46 07.825730	+24 56 32.52437	0.7467	Q	17.1
J0057+3021	0055+300	NGC 315	A	00 57 48.883342	+30 21 08.81194	0.0165	G	12.2
J0102+5824	0059+581	7C 0059+5808	B	01 02 45.762380	+58 24 11.13659	0.6440	Q	17.6
J0109+6133	0106+612		B	01 09 46.344370	+61 33 30.45531	0.7830	G	19.4
J0112+3522	0109+351		A	01 12 12.944409	+35 22 19.33615	0.4500	Q	17.8
J0113+4948	0110+495		A	01 13 27.006813	+49 48 24.04306	0.3890	Q	18.4
J0126+7046	0122+705		B	01 26 7.8495750	+70 46 52.38656	...	U	18.7
J0136+4751	0133+476	DA 55	B,C	01 36 58.594700	+47 51 29.10000	0.8590	Q	18.0
J0137+2145	0134+215		A	01 37 15.624949	+21 45 44.27088	...	U	...
J0154+4743	0151+474		B	01 54 56.289889	+47 43 26.53956	1.0260	Q	...
J0205+3212	0202+319		A	02 05 04.925360	+32 12 30.09541	1.4660	Q	18.2
J0253+3217	0250+320		A	02 53 33.650138	+32 17 20.89168	0.8590	Q	...
J0254+2343	0251+235		A	02 54 24.718127	+23 43 26.47461	1.9870	Q	...
J0310+3814	0307+380		B	03 10 49.879930	+38 14 53.83778	0.9450	Q	18.5
J0313+4120	0309+411	NRAO 128	B	03 13 01.962125	+41 20 01.18349	0.1340	G	18.0
J0319+4130	0316+413	3C 84	A,B,C	03 19 48.160100	+59 33 22.21466	0.0176	G	12.6
J0325+2224	0322+222		C	03 25 36.814357	+22 24 00.36551	2.0660	Q	18.9
J0325+4655	0321+467		C	03 25 20.303800	+46 55 06.63500	...	B	14.1
J0333+6536	0329+654		C	03 33 56.737600	+65 36 56.18400	...	B	19.3
J0344+6827	0339+683		A,C	03 44 41.441278	+68 27 47.81028	...	U	...
J0359+3220	0356+322		A	03 59 44.912917	+32 20 47.15548	1.3310	Q	19.9
J0359+5057	0355+508	NRAO 150	A	03 59 29.747200	+50 57 50.16100	1.5200	Q	22.9
J0428+3259	0424+328		A	04 28 05.808725	+32 59 52.04381	0.4760	Q	20.2
J0512+4041	0509+406		A	05 12 52.542864	+40 41 43.62019	...	Q	...
J0533+4822	0529+483		A	05 33 15.865792	+48 22 52.80771	1.1620	Q	19.9
J0604+2429	0601+245	4C 24.11	A	06 04 55.121380	+24 29 55.03635	1.1330	G	...
J0612+4122	0609+413		A	06 12 51.185236	+41 22 37.40815	...	B	15.7
J0618+4207	0614+421		A	06 18 08.619909	+42 07 59.84609	...	U	...
J0632+3200	0629+320		A	06 32 30.782861	+32 00 53.63193	1.8310	Q	...
J0638+5933	0633+595		B	06 38 02.871950	+59 33 22.21466	...	B	...
J0639+7324	0633+734		C	06 39 21.961200	+73 24 58.04000	1.8500	Q	17.8
J0642+8811	0604+882		C	06 42 6.1363170	+88 11 55.01734	...	B	19.5
J0650+6001	0646+600		B	06 50 31.254355	+60 01 44.55601	0.4550	Q	18.9
J0700+1709	0657+172		A	07 00 01.525539	+17 09 21.70130	...	U	21.0
J0707+6110	0702+612		B	07 07 00.615678	+61 10 11.60689	...	U	17.0
J0713+1935	0710+196	WB92 0711+1940	A	07 13 30.782861	+19 35 00.40875	0.5400	Q	18.6
J0721+7120	0716+714	S5 0716+71	B,C	07 21 53.448400	+71 20 36.36300	0.3000	B	15.5
J0733+5022	0730+504		C	07 33 52.520500	+50 22 09.06200	0.7200	Q	19.0
J0741+3112	0738+313	OI 363	C	07 41 10.703310	+31 12 00.22894	0.6320	Q	16.7
J0747+7639	0740+767		B	07 47 14.607565	+76 39 17.27140	...	B	20.0
J0748+2400	0745+241	S3 0745+24	C	07 48 36.109275	+24 00 24.11002	0.4092	Q	19.7
J0753+5352	0749+540	4C 54.15	C	07 53 01.384569	+53 52 59.63709	0.2000	B	18.5
J0808+4052	0805+410		C	08 08 56.652043	+40 52 44.88880	1.4193	Q	19.0
J0809+5341	0805+538		C	08 09 41.732819	+53 41 25.09245	2.1330	Q	19.8
J0814+6431	0810+646		C	08 14 39.190224	+64 31 22.02696	...	B	17.9
J0815+3635	0812+367		C	08 15 25.944861	+36 35 15.14876	1.0286	Q	18.0
J0817+3227	0814+326		C	08 17 28.542305	+32 27 02.92601	...	G	21.6
J0824+3916	0821+394	4C 39.23	C	08 24 55.483855	+39 16 41.90401	1.2159	Q	18.3
J0854+2006	0851+202	OJ 287	B	08 54 48.874900	+20 06 30.64100	0.3060	B	14.0
J0909+4253	0906+430		A	09 09 33.497140	+42 53 46.48213	0.6704	G	20.0
J0917+6530	0913+657		C	09 17 55.568093	+65 30 15.12741	...	U	...
J0920+4441	0917+449		A	09 20 58.458486	+44 41 53.98499	2.1890	Q	18.1
J0925+3612	0922+364		A	09 25 51.851387	+36 12 35.67435	1.0150	U	19.3
J0927+3902	0923+392	4C 39.25	C	09 27 03.013934	+39 02 20.85186	0.6950	Q	17.9
J0937+5008	0933+503		C	09 37 13.327300	+50 08 52.09700	0.2757	G	18.9
J0945+3534	0942+358		A	09 45 38.120719	+35 34 55.08842	1.1283	Q	18.8
J0956+2515	0953+254	OK 290	A	09 56 49.875378	+25 15 16.04976	0.7120	Q	17.5
J0957+5522	0954+556		C	09 57 38.184500	+55 22 57.76800	0.8990	B	17.7
J0958+4725	0955+476	OK 492	C	09 58 19.671640	+47 25 07.84244	1.8815	Q	18.8
J1013+2449	1011+250		A	10 13 53.428771	+24 49 16.44062	1.6360	Q	15.4
J1018+3542	1015+359	B2 1015+35B	C	10 18 10.988093	+35 42 39.44094	1.2280	Q	18.6
J1033+4116	1030+415		C	10 33 03.707872	+41 16 06.23282	1.1185	Q	19.6
J1033+6051	1030+611		C	10 33 51.428900	+60 51 07.33500	1.4010	Q	18.9
J1038+4244	1035+430		C	10 38 18.190536	+42 44 42.75990	0.3055	Q	18.4
J1043+2408	1040+244	B2 1040+24A	A	10 43 09.035778	+24 08 35.40922	0.5590	Q	17.7
J1044+8054	1039+811		B	10 44 23.062546	+80 54 39.44301	1.2600	Q	16.5
J1045+1735	1042+178		A	10 45 14.359788	+17 35 48.08359	0.9210	U	21.8
J1058+8114	1053+815		B	10 58 11.535395	+81 14 32.67511	0.7060	Q	18.5
J1103+3014	1100+305		B	11 03 13.301905	+30 14 42.70196	0.3838	G	18.3

**Table 5.** List of Sources (*continued*)

Source (J2000) (1)	Source (B1950) (2)	Common Name (3)	Epoch (4)	$\alpha_{2000}$ (5)	$\delta_{2000}$ (6)	$z$ (7)	Type (8)	$m_v$ (9)
J1130+3815	1128+385		B	11 30 53.282615	+38 15 18.54688	1.7330	Q	18.6
J1146+3958	1144+402		B	11 46 58.297920	+39 58 34.30434	1.0880	Q	18.0
J1152+4939	1149+499		B	11 52 32.871056	+49 39 38.76785	1.0931	Q	16.6
J1153+4931	1150+497	4C 49.22	B	11 53 24.466600	+49 31 08.83000	0.3334	Q	17.1
J1153+8058	1150+812		B	11 53 12.499212	+80 58 29.15456	1.2500	Q	18.5
J1200+5300	1157+532		C	12 00 11.384309	+53 00 46.87708	1.9970	Q	19.7
J1203+4803	1200+483		C	12 03 29.853038	+48 03 13.62592	0.8133	G	16.4
J1219+6344	1216+640		C	12 19 10.583100	+63 44 10.71688	...	U	22.5
J1224+2122	1222+216	4C 21.35	A	12 24 54.458398	+21 22 46.38854	0.4335	Q	17.5
J1229+0203	1226+023	3C 273B	A,B	12 29 06.699700	+02 03 08.59800	0.1583	B	12.9
J1241+5458	1239+552		C	12 41 27.703846	+54 58 19.05549	...	U	22.1
J1256-0547	1253-055	3C 279	B	12 56 11.166500	-05 47 21.52500	0.5362	Q	15.2
J1259+5140	1257+515		C	12 59 31.173983	+51 40 56.26083	...	U	19.9
J1306+5529	1303+557		C	13 06 03.351107	+55 29 43.85746	1.6000	G	17.5
J1310+3220	1308+326	OP 313	B	13 10 28.663800	+32 20 43.78200	0.9970	Q	19.0
J1327+2210	1324+224	B2 1324+22	A	13 27 00.861314	+22 10 50.16277	1.4034	Q	17.2
J1329+3154	1327+321		A	13 29 52.864909	+31 54 11.05443	0.3350	B	20.0
J1341+2816	1338+285		A	13 41 15.282755	+28 16 05.07702	1.2750	Q	19.6
J1353+7532	1352+757		B	13 53 23.168007	+75 32 57.73527	1.6190	Q	17.7
J1357+7643	1357+769		B	13 57 55.371536	+76 43 21.05098	1.5850	Q	19.0
J1407+2827	1404+286	OQ 208	A	14 07 00.394415	+28 27 14.69008	0.0766	G	16.0
J1419+3821	1417+385		A	14 19 46.613761	+38 21 48.47496	1.8320	Q	19.3
J1506+4239	1505+428		A	15 06 53.041839	+42 39 23.03555	0.5870	Q	21.5
J1506+8319	1510+835		B	15 06 24.715438	+83 19 28.03538	2.5770	Q	18.7
J1521+4336	1520+437		A	15 21 49.613879	+43 36 39.26807	2.1750	Q	18.4
J1549+5038	1547+507		C	15 49 17.468558	+50 38 05.78820	2.1741	Q	18.9
J1608+4012	1606+403	5C 13.225	B	16 08 22.157698	+40 12 17.83288	0.6275	Q	20.8
J1624+5741	1623+578		C	16 24 24.807566	+57 41 16.28100	0.7890	G	17.3
J1635+3808	1633+382	4C 38.41	C	16 35 15.492900	+38 08 04.50000	1.8130	Q	17.7
J1637+4717	1636+473	4C 47.44	B	16 37 45.130554	+47 17 33.83090	0.7350	Q	17.5
J1640+3946	1638+398		B	16 40 29.632770	+39 46 46.02835	1.6660	Q	18.5
J1642+3948	1641+399	3C 345	A,B	16 42 58.809900	+39 48 36.99300	0.5950	B	16.5
J1646+4059	1645+410		B	16 46 56.858690	+40 59 17.17204	0.8350	Q	20.7
J1653+3107	1651+312		A	16 53 29.910650	+31 07 56.87239	1.2954	Q	13.6
J1659+2629	1657+265	4C 26.51	A	16 59 24.149448	+26 29 36.94297	0.7947	Q	18.0
J1701+3954	1659+399		A	17 01 24.634812	+39 54 37.09149	0.5071	B	17.4
J1716+6836	1716+686		C	17 16 13.938009	+68 36 38.74465	0.7770	Q	18.5
J1726+3213	1724+322		A	17 26 35.124676	+32 13 23.02210	1.0900	G	16.0
J1735+5049	1734+508		A	17 35 49.005166	+50 49 11.56578	0.8350	G	23.1
J1746+6226	1745+624	4C 62.29	B	17 46 14.034133	+62 26 54.73830	3.8890	Q	19.5
J1751+2920	1749+293		A	17 51 42.683934	+29 20 50.20228	...	U	...
J1753+2848	1751+288		A	17 53 42.473647	+28 48 04.93877	1.1180	Q	19.6
J1800+3848	1758+388		A	18 00 24.765361	+38 48 30.69742	2.0920	Q	18.0
J1800+7828	1803+784		C	18 00 45.683900	+78 28 04.01800	0.6797	B	17.0
J1808+4542	1806+456		C	18 08 21.885884	+45 42 20.86639	0.8300	Q	19.3
J1811+1704	1809+170		A	18 11 43.183465	+17 04 57.25713	...	Q	20.5
J1821+6818	1822+682	B,C	18 21 59.491723	+68 18 43.00867	1.6920	G	...	
J1823+6857	1823+689	B	18 23 32.853905	+68 57 52.61247	...	B	19.0	
J1849+6705	1849+670	B	18 49 16.072283	+67 05 41.68022	0.6570	Q	18.6	
J1850+2825	1848+283	A	18 50 27.589824	+28 25 13.15527	2.5600	Q	17.1	
J1922+1530	1920+154		A	19 22 34.699313	+15 30 10.03193	...	U	...
J1927+6117	1926+611		C	19 27 30.442616	+61 17 32.87881	0.4730	B	17.5
J1930+1532	1928+154	4C 15.66	A	19 30 52.766983	+15 32 34.42704	...	U	...
J1933+6540	1933+655		C	19 33 57.337206	+65 40 16.82845	1.6870	Q	18.7
J1939+3817	1937+381		B	19 39 33.566865	+38 17 35.38833	...	U	17.5
J1955+5131	1954+513	OV 591	B	19 55 42.738264	+51 31 48.54602	1.2230	Q	18.5
J2002+1501	2000+148		C	20 02 41.999236	+15 01 14.57396	...	U	...
J2002+4725	2000+472		B	20 02 10.418256	+47 25 28.77372	2.2660	Q	19.6
J2007+3722	2005+372		B	20 07 45.397822	+37 22 02.31078	...	U	...
J2012+4628	2010+463	7C 2010+4619	C	20 12 05.637418	+46 28 55.77715	...	B	18.2
J2015+3410	2013+340		C	20 15 28.831879	+34 10 39.40992	...	B	...
J2015+3710	2013+370	B,C	20 15 28.729778	+37 10 59.51495	0.8590	B	21.8	
J2016+1632	2013+163	C	20 16 13.860029	+16 32 34.11306	...	B	1.0	
J2016+3600	2014+358	A	20 16 45.618743	+36 00 33.37332	...	U	...	
J2017+7440	2017+745	4C 74.25	A	20 17 13.079301	+74 40 47.99898	2.1870	Q	18.3
J2022+6136	2021+614	OW 637	A	20 22 06.681758	+61 36 58.80486	0.2270	G	19.5
J2022+7611	2023+760		A	20 22 35.575939	+76 11 26.17158	0.5940	B	17.8
J2024+1718	2022+171		C	20 24 56.563449	+17 18 13.19767	1.0500	Q	17.5
J2051+1743	2049+175		C	20 51 35.582921	+17 43 36.90076	0.1950	G	18.0
J2109+3532	2107+353	B2 2107+35A	A	21 09 31.878718	+35 32 57.59746	0.2023	G	13.9
J2114+4634	2112+463		A	21 14 32.875692	+46 34 39.30126	...	U	...
J2137+5101	2135+508		A	21 37 00.986190	+51 01 36.12894	...	U	...
J2154+1727	2152+172		C	21 54 40.900400	+17 27 50.79300	1.0200	Q	18.0
J2202+4216	2200+420	BL Lac	A,C	22 02 43.291371	+42 16 39.97992	0.0686	B	14.5

**Table 5.** List of Sources (*continued*)

Source (J2000) (1)	Source (B1950) (2)	Common Name (3)	Epoch (4)	$\alpha_{2000}$ (5)	$\delta_{2000}$ (6)	$z$ (7)	Type (8)	$m_V$ (9)
J2203+1725	2201+171		C	22 03 26.893600	+17 25 48.24700	1.0760	Q	18.8
J2203+3145	2201+315	4C 31.63	C	22 03 14.975700	+31 45 38.26900	0.2950	Q	15.5
J2210+2013	2208+199		A	22 10 51.652453	+20 13 24.05454	0.2820	Q	...
J2212+2355	2209+236		A	22 12 05.966311	+23 55 40.54372	1.1250	Q	19.0
J2217+2421	2214+241		C	22 17 00.821100	+24 21 45.95700	0.5050	B	17.2
J2218+1520	2215+150		A	22 18 10.913904	+15 20 35.71746	2.3350	Q	...
J2253+1608	2251+158	3C 454.3	A,B,C	22 53 57.747937	+16 08 53.56094	0.8590	B	16.1
J2305+8242	2304+824		A	23 05 17.539999	+82 42 49.15557	0.6200	B	...
J2311+4543	2309+454		A	23 11 47.408964	+45 43 56.01658	1.4470	Q	...
J2312+7241	2310+724		C	23 12 19.697802	+72 41 26.91735	...	U	19.3
J2322+4445	2319+444		A	23 22 20.358080	+44 45 42.35353	1.3100	U	20.7
J2322+5057	2320+506		A	23 22 25.982171	+50 57 51.96363	1.2790	Q	18.6
J2330+3348	2327+335		C	23 30 13.737652	+33 48 36.47152	1.8090	Q	18.5
J2354+4553	2351+456	4C 45.51	A	23 54 21.680218	+45 53 04.23640	1.9860	Q	20.6

**Columns:** 1 – IAU Source name (J2000); 2 – IAU Source name (B1950); 3 – common name; 4 – observing epochs – A: October 2010; B: May 2011 and C: October 2011; 5,6 – source coordinates in J2000 epoch: right ascension and declination; 7 – redshift; 8 – optical class – Q: quasar; B: BL Lac object; G: Galaxy; U: Unidentified source; 9 – optical V magnitude (information for Columns 7,8,9 obtained from the Simbad Astronomical Database (<http://simbad.u-strasbg.fr/simbad>; Wenger et al. 2000), Sloan Digital Sky Survey (<http://www.sdss.org/>) and NASA/IPAC Extragalactic Database (<https://ned.ipac.caltech.edu>); (This table is also available in a machine-readable and Virtual Observatory (VO) forms in the online journal.)

**Table 6.** Image Parameters

Source (J2000)	Obs (1)	$S_{86\text{GHz}}$ (2)	$S_S$ (3)	$B_S$ (4)	$S_L$ (5)	$B_L$ (6)	$B_a$ (7)	$B_b$ (8)	$B_{PA}$ (9)	$S_t$ (10)	$S_p$ (11)	$\sigma$ (12)	$\xi_r$ (13)
J0013+4051	C	0.79	$0.656 \pm 0.020$	56	$0.192 \pm 0.006$	3136	159	35	-16.8	436	317	8	1.43
J0017+8135	B	0.18	$0.263 \pm 0.018$	60	$0.075 \pm 0.004$	3062	74	35	62.1	143	81	2	1.36
J0030+7037	B	0.34	$0.363 \pm 0.026$	65	$0.115 \pm 0.009$	3070	76	36	66.5	155	92	3	1.34
J0034+2754	C	0.07	$0.124 \pm 0.015$	54	$0.156 \pm 0.021$	3086	262	36	-14.2	159	60	2	1.04
J0044+6803	B	0.17	$0.315 \pm 0.023$	65	$0.097 \pm 0.006$	3034	75	36	70.4	133	99	3	1.15
J0046+2456	A	0.47	$0.252 \pm 0.019$	59	$0.137 \pm 0.009$	3060	267	37	-15.0	235	160	6	1.17
J0057+3021	A	0.48	$0.361 \pm 0.023$	58	$0.233 \pm 0.017$	3060	308	37	-14.5	306	226	8	1.07
J0102+5824	B	3.11	$3.579 \pm 0.037$	44	$0.336 \pm 0.020$	3050	59	43	-19.5	2221	1075	19	1.58
J0109+6133	B	0.64	$0.706 \pm 0.026$	45	$0.242 \pm 0.023$	3048	111	37	-12.9	381	239	5	1.17
J0112+3522	A	0.53	$0.624 \pm 0.031$	58	$0.105 \pm 0.008$	3054	205	37	-18.3	238	119	3	1.08
J0113+4948	A	0.61	$0.547 \pm 0.026$	56	$0.156 \pm 0.011$	3066	119	36	-28.2	269	234	9	1.32
J0126+7046	B	0.07	$0.233 \pm 0.018$	48	$0.071 \pm 0.004$	2474	115	36	-13.4	76	69	2	1.20
J0136+4751	B	1.95	$2.531 \pm 0.060$	33	$1.324 \pm 0.037$	2388	157	43	-14.4	2090	862	14	1.21
J0136+4751	C	1.76	$1.811 \pm 0.026$	46	$0.518 \pm 0.045$	2870	230	36	-0.5	1317	740	15	1.15
J0137+2145	A	0.07	$0.289 \pm 0.018$	54	$0.184 \pm 0.007$	3070	259	40	-10.2	278	175	3	1.03
J0154+4743	B	...	$0.436 \pm 0.022$	32	$0.315 \pm 0.026$	2860	150	42	-11.2	239	172	4	1.12
J0205+3212	A	0.81	$0.530 \pm 0.037$	49	$0.228 \pm 0.019$	3052	185	38	-11.6	499	182	4	1.09
J0253+3217	A	0.37	$0.579 \pm 0.032$	43	$0.276 \pm 0.014$	3070	190	39	-9.0	259	205	5	1.01
J0254+2343	A	0.05	$0.342 \pm 0.035$	48	$0.340 \pm 0.027$	3060	245	39	-8.7	186	170	5	0.99
J0310+3814	B	0.44	$0.320 \pm 0.017$	58	$0.272 \pm 0.021$	3050	193	40	-29.3	190	182	9	1.35
J0313+4120	B	0.89	$0.823 \pm 0.031$	58	$0.294 \pm 0.018$	3020	178	39	-30.9	663	349	8	1.26
J0319+4130	A	12.06	$4.690 \pm 0.181$	26	$0.506 \pm 0.054$	3064	155	33	-12.2	7677	978	10	1.16
J0319+4130	B	12.15	$9.885 \pm 0.206$	55	$0.357 \pm 0.074$	2972	170	44	-24.1	8865	724	9	1.12
J0319+4130	C	13.85	$3.290 \pm 0.126$	67	$0.158 \pm 0.017$	1634	185	116	2.7	3504	625	6	0.66
J0325+2224	C	0.90	$0.879 \pm 0.037$	39	$0.266 \pm 0.010$	3131	203	37	-9.0	621	370	12	1.12
J0325+4655	C	0.27	$0.258 \pm 0.018$	33	$0.074 \pm 0.008$	3135	127	40	-9.3	190	88	4	0.81
J0333+6536	C	0.07	$0.189 \pm 0.020$	40	$0.158 \pm 0.013$	3050	109	37	-12.0	77	64	3	1.04
J0344+6827	A	0.06	$0.187 \pm 0.023$	62	$0.136 \pm 0.007$	3138	122	39	-35.5	105	97	3	1.10
J0344+6827	C	0.07	$0.213 \pm 0.017$	41	$0.205 \pm 0.018$	3030	105	35	-7.7	159	66	2	1.20
J0359+3220	A	0.36	$0.358 \pm 0.037$	67	$0.140 \pm 0.021$	3132	173	43	-12.6	318	140	2	1.05
J0359+5057	A	...	$1.861 \pm 0.076$	67	$0.336 \pm 0.011$	3058	148	40	-48.6	1477	313	23	1.12
J0428+3259	A	0.04	$0.325 \pm 0.025$	67	$0.131 \pm 0.009$	3138	167	45	-11.4	124	103	5	0.94
J0512+4041	A	1.29	$1.014 \pm 0.035$	53	$0.211 \pm 0.009$	3070	159	38	-22.7	409	235	4	1.63
J0533+4822	A	1.26	$1.807 \pm 0.027$	51	$0.417 \pm 0.008$	3065	138	38	-25.7	556	258	7	1.28
J0604+2429	A	0.20	$0.313 \pm 0.024$	48	$0.188 \pm 0.008$	2474	262	35	-10.7	247	203	4	1.07
J0612+4122	A	0.27	$0.361 \pm 0.025$	48	$0.155 \pm 0.010$	3060	154	39	-19.4	260	167	2	1.17
J0618+4207	A	0.05	$0.277 \pm 0.031$	49	$0.151 \pm 0.006$	3055	148	38	-18.8	154	147	2	1.12
J0632+3200	A	0.02	$0.350 \pm 0.028$	44	$0.168 \pm 0.006$	2473	208	37	-11.0	174	174	6	1.01
J0638+5933	B	0.39	$0.264 \pm 0.018$	42	$0.074 \pm 0.006$	3140	109	37	-22.7	130	74	3	0.94
J0639+7324	C	0.56	$0.213 \pm 0.012$	46	$0.186 \pm 0.016$	2992	87	38	14.5	374	131	5	0.94
J0642+8811	C	0.15	$0.251 \pm 0.014$	56	$0.096 \pm 0.008$	3091	85	37	26.5	121	74	3	1.02
J0650+6001	B	0.26	$0.287 \pm 0.023$	40	$0.091 \pm 0.005$	3062	94	36	-20.6	149	92	4	0.99
J0700+1709	A	1.05	$0.863 \pm 0.040$	47	$0.138 \pm 0.008$	2471	323	37	-7.9	630	234	6	1.05
J0707+6110	B	0.23	$0.267 \pm 0.020$	38	$0.090 \pm 0.005$	3040	93	36	-14.7	164	94	2	1.14
J0713+1935	A	0.23	$0.416 \pm 0.036$	46	$0.210 \pm 0.007$	2471	329	37	-5.8	220	216	10	0.79
J0721+7120	B	4.91	$1.216 \pm 0.105$	43	$0.533 \pm 0.028$	3135	55	40	-65.9	2935	1284	25	1.44
J0721+7120	C	...	$1.309 \pm 0.039$	39	$0.859 \pm 0.017$	3138	55	39	-17.9	1119	980	22	0.70
J0733+5022	C	0.26	$0.364 \pm 0.023$	23	$0.112 \pm 0.007$	2472	119	42	12.6	156	109	4	1.04
J0741+3112	C	0.43	$0.417 \pm 0.020$	42	$0.413 \pm 0.025$	3081	191	39	-2.5	451	268	7	1.03
J0747+7639	B	0.12	$0.291 \pm 0.023$	47	$0.090 \pm 0.007$	3080	105	38	-2.1	58	59	2	1.03
J0748+2400	C	0.88	$0.522 \pm 0.029$	45	$0.253 \pm 0.008$	3116	185	38	-7.6	1002	421	11	1.05
J0753+5352	C	0.49	$0.690 \pm 0.055$	25	$0.526 \pm 0.059$	2760	106	40	10.0	483	328	8	1.16
J0808+4052	C	0.51	$0.415 \pm 0.031$	34	$0.199 \pm 0.008$	3135	123	36	-3.2	361	247	4	1.30
J0809+5341	C	0.11	$0.217 \pm 0.014$	35	$0.180 \pm 0.020$	3084	120	40	10.0	100	93	4	1.07
J0814+6431	C	...	$0.360 \pm 0.023$	45	$0.290 \pm 0.025$	3087	95	41	-12.6	370	324	5	1.35
J0815+3635	C	...	$0.444 \pm 0.024$	44	$0.454 \pm 0.038$	3050	173	41	-11.8	427	370	7	1.04
J0817+3227	C	...	$0.443 \pm 0.022$	46	$0.461 \pm 0.024$	3020	207	45	-5.1	527	379	6	1.00
J0824+3916	C	...	$0.320 \pm 0.021$	45	$0.209 \pm 0.009$	3075	128	36	-10.5	369	244	3	1.02
J0854+2006	B	6.70	$0.854 \pm 0.111$	64	$0.889 \pm 0.044$	3128	301	37	-14.5	4274	1317	58	1.24
J0909+4253	A	0.67	$0.378 \pm 0.023$	53	$0.146 \pm 0.011$	3070	148	38	-20.9	232	155	2	1.14
J0917+6530	C	0.01	$0.235 \pm 0.022$	50	$0.318 \pm 0.013$	3085	108	38	-7.1	245	187	15	0.76
J0920+4441	A	1.89	$2.866 \pm 0.037$	53	$0.392 \pm 0.010$	3070	140	38	-22.8	1018	390	11	1.54
J0925+3612	A	0.12	$0.227 \pm 0.020$	56	$0.136 \pm 0.008$	3062	176	44	-19.5	258	203	4	1.12
J0927+3902	C	...	$3.907 \pm 0.055$	48	$0.694 \pm 0.062$	3086	200	37	-4.2	3286	447	6	1.15
J0937+5008	C	0.53	$0.393 \pm 0.027$	49	$0.353 \pm 0.028$	3088	135	37	-6.7	349	322	11	0.97
J0945+3534	A	0.04	$0.219 \pm 0.026$	55	$0.163 \pm 0.011$	3065	188	40	-15.9	186	157	4	1.06
J0956+2515	A	1.03	$0.610 \pm 0.030$	50	$0.300 \pm 0.010$	3050	239	36	-13.6	593	373	9	1.12
J0957+5522	C	0.54	$0.244 \pm 0.021$	47	$0.342 \pm 0.013$	3087	116	38	-7.2	306	236	11	0.83
J0958+4725	C	0.37	$0.389 \pm 0.028$	49	$0.224 \pm 0.009$	3134	107	39	-17.0	368	251	5	1.37
J1013+2449	A	0.11	$0.254 \pm 0.031$	49	$0.228 \pm 0.009$	3050	255	36	-12.7	240	201	5	1.18
J1018+3542	C	0.50	$0.351 \pm 0.030$	30	$0.387 \pm 0.024$	2980	163	37	-4.1	434	378	8	0.98
J1033+4116	C	0.92	$$										

**Table 6.** Image Parameters *continued*

Source (J2000)	Obs	$S_{\text{86 GHz}}$	$S_{\text{S}}$	$B_{\text{S}}$	$S_{\text{L}}$	$B_{\text{L}}$	$B_{\text{a}}$	$B_{\text{b}}$	$B_{\text{PA}}$	$S_{\text{t}}$	$S_{\text{p}}$	$\sigma$	$\xi_{\text{r}}$
(1)	(2)	(3)	(4)	(5)	(6)	(7)	(8)	(9)	(10)	(11)	(12)	(13)	(14)
J1038+4244	C	0.15	$0.314 \pm 0.027$	30	$0.241 \pm 0.011$	2975	150	37	-2.9	191	184	6	1.01
J1043+2408	A	0.92	$0.914 \pm 0.037$	47	$0.331 \pm 0.016$	3020	300	36	-9.3	631	421	16	1.02
J1044+8054	B	1.08	$1.433 \pm 0.027$	56	$0.126 \pm 0.013$	3052	104	33	-41.1	776	289	4	1.22
J1045+1735	A	0.28	$0.368 \pm 0.034$	52	$0.302 \pm 0.011$	3054	351	38	-8.9	339	243	6	0.94
J1058+8114	B	0.76	$0.955 \pm 0.027$	56	$0.177 \pm 0.008$	3036	98	34	-40.1	571	264	5	1.20
J1103+3014	B	0.48	$0.471 \pm 0.024$	48	$0.230 \pm 0.008$	2474	220	42	-1.8	482	250	5	1.12
J1130+3815	B	1.00	$1.061 \pm 0.029$	39	$0.246 \pm 0.007$	2456	196	42	-5.7	720	255	7	1.18
J1146+3958	B	1.60	$1.970 \pm 0.033$	34	$0.857 \pm 0.007$	2420	229	37	6.8	1479	697	19	1.15
J1152+4939	B	0.12	$0.302 \pm 0.016$	33	$0.090 \pm 0.008$	2400	200	36	12.3	83	75	4	0.96
J1153+4931	B	2.30	$1.252 \pm 0.081$	31	$1.880 \pm 0.017$	2384	179	37	17.3	1518	1030	39	1.20
J1153+8058	B	0.41	$0.406 \pm 0.025$	55	$0.088 \pm 0.006$	3114	101	36	-25.9	153	82	2	1.10
J1200+5300	C	0.08	$0.121 \pm 0.011$	53	$0.365 \pm 0.025$	3080	125	36	-16.5	106	85	3	1.25
J1203+4803	C	0.34	$0.225 \pm 0.018$	52	$0.207 \pm 0.020$	3085	135	36	-10.4	135	94	3	1.33
J1219+6344	C	0.03	$0.136 \pm 0.009$	54	$0.222 \pm 0.020$	3058	162	35	-14.8	67	66	5	0.94
J1224+2122	A	...	$1.715 \pm 0.036$	63	$0.348 \pm 0.023$	2970	255	83	-19.9	1205	494	17	0.90
J1229+0203	A	16.21	$3.242 \pm 0.079$	69	$0.404 \pm 0.040$	1460	383	138	-22.9	4523	1425	68	1.01
J1229+0203	B	11.41	$5.094 \pm 0.095$	156	$0.149 \pm 0.024$	575	1277	188	-34.8	2482	1510	76	0.83
J1241+5458	C	...	$0.165 \pm 0.012$	53	$0.206 \pm 0.019$	3010	149	37	-12.2	71	66	4	1.28
J1256-0547	B	22.96	$18.827 \pm 0.980$	37	$1.689 \pm 0.049$	1676	311	91	-21.8	22696	7250	205	1.16
J1259+5140	C	0.29	$0.144 \pm 0.014$	54	$0.364 \pm 0.048$	2890	114	38	-14.7	189	141	7	1.08
J1306+5529	C	0.08	$0.159 \pm 0.013$	61	$0.075 \pm 0.009$	2469	98	42	-27.5	77	59	3	1.00
J1310+3220	B	1.37	$1.422 \pm 0.065$	39	$0.233 \pm 0.018$	3052	179	37	-8.4	798	247	9	0.98
J1327+2210	A	...	$0.575 \pm 0.044$	57	$0.214 \pm 0.015$	3060	305	43	-16.7	391	288	5	1.00
J1329+3154	A	0.38	$0.348 \pm 0.032$	57	$0.190 \pm 0.011$	3046	203	35	-16.1	297	202	4	1.01
J1341+2816	A	0.14	$0.310 \pm 0.023$	58	$0.232 \pm 0.008$	3054	235	36	-15.6	235	203	6	0.90
J1353+7532	B	0.13	$0.286 \pm 0.023$	48	$0.087 \pm 0.005$	2988	104	35	-0.2	91	73	2	1.40
J1357+7643	B	0.31	$0.371 \pm 0.024$	49	$0.147 \pm 0.008$	2994	107	34	-0.6	177	175	4	1.35
J1407+2827	A	0.02	$0.368 \pm 0.021$	47	$0.218 \pm 0.009$	3066	249	37	-12.6	251	189	5	1.03
J1419+3821	A	0.49	$0.498 \pm 0.027$	45	$0.186 \pm 0.027$	2840	234	36	-12.3	223	142	7	1.16
J1506+4239	A	0.56	$0.434 \pm 0.027$	39	$0.143 \pm 0.015$	2946	201	30	-4.7	183	201	8	1.27
J1506+8319	B	0.11	$0.276 \pm 0.019$	52	$0.092 \pm 0.007$	2974	105	35	17.2	83	69	2	1.21
J1521+4336	A	0.37	$0.315 \pm 0.028$	39	$0.208 \pm 0.010$	3054	153	34	-7.7	212	211	9	1.37
J1549+5038	C	0.31	$0.268 \pm 0.019$	46	$0.191 \pm 0.010$	2440	263	35	4.3	320	253	5	1.03
J1608+4012	B	0.46	$0.786 \pm 0.026$	54	$0.232 \pm 0.009$	3070	190	35	-17.7	303	304	11	1.40
J1624+5741	C	0.32	$0.257 \pm 0.023$	36	$0.179 \pm 0.005$	2412	204	37	13.6	370	255	5	1.03
J1635+3808	C	2.65	$1.036 \pm 0.099$	32	$0.814 \pm 0.014$	2305	226	37	13.0	1676	1133	24	1.15
J1637+4717	B	1.01	$1.098 \pm 0.024$	48	$0.201 \pm 0.018$	3044	189	34	-14.8	751	407	6	1.34
J1640+3946	B	1.00	$1.105 \pm 0.022$	46	$0.158 \pm 0.015$	3030	190	35	-8.9	630	265	4	1.14
J1642+3948	A	4.58	$2.192 \pm 0.154$	61	$0.194 \pm 0.011$	3026	242	34	-16.6	1104	423	27	0.97
J1642+3948	B	3.68	$3.689 \pm 0.054$	42	$0.419 \pm 0.021$	2984	204	34	-6.9	2563	705	12	1.21
J1646+4059	B	0.16	$0.309 \pm 0.015$	44	$0.141 \pm 0.009$	3000	184	36	-7.8	87	68	2	1.06
J1653+3107	A	0.31	$0.380 \pm 0.026$	54	$0.195 \pm 0.013$	2474	207	43	-11.2	327	165	1	1.14
J1659+2629	A	0.35	$0.310 \pm 0.028$	57	$0.203 \pm 0.013$	2476	234	42	-10.9	311	147	2	1.10
J1701+3954	A	0.30	$0.355 \pm 0.021$	55	$0.176 \pm 0.011$	2476	158	41	-19.6	232	151	2	1.21
J1716+6836	C	0.36	$0.334 \pm 0.030$	40	$0.817 \pm 0.058$	2786	185	35	26.4	252	227	10	1.24
J1726+3213	A	0.12	$0.313 \pm 0.023$	52	$0.180 \pm 0.008$	2470	237	36	-15.6	176	177	5	0.86
J1735+5049	A	0.22	$0.230 \pm 0.035$	51	$0.157 \pm 0.005$	2469	139	43	-20.5	229	150	2	1.07
J1746+6226	B	0.08	$0.207 \pm 0.016$	64	$0.100 \pm 0.006$	3016	89	38	-69.0	94	71	2	1.20
J1751+2920	A	0.44	$0.490 \pm 0.030$	52	$0.196 \pm 0.009$	2464	256	36	-14.4	340	257	7	1.10
J1753+2848	A	0.35	$0.362 \pm 0.038$	54	$0.115 \pm 0.012$	2472	353	38	-11.5	192	154	6	0.96
J1800+3848	A	0.30	$0.344 \pm 0.028$	53	$0.178 \pm 0.011$	2444	221	36	-18.2	228	200	6	0.88
J1800+7828	C	2.36	$2.847 \pm 0.075$	53	$0.282 \pm 0.012$	3134	46	43	-35.7	1736	548	11	1.13
J1808+4542	C	0.44	$0.373 \pm 0.038$	18	$0.402 \pm 0.031$	2140	205	73	35.6	183	181	9	0.93
J1811+1704	A	0.42	$0.343 \pm 0.050$	58	$0.379 \pm 0.025$	3030	383	37	-7.9	379	268	7	0.99
J1821+6818	B	0.33	$0.315 \pm 0.022$	62	$0.125 \pm 0.009$	3061	82	37	-64.2	199	145	4	1.18
J1821+6818	C	0.25	$0.176 \pm 0.021$	51	$0.168 \pm 0.009$	3116	161	35	-24.9	220	179	4	1.17
J1823+6857	B	0.10	$0.213 \pm 0.016$	62	$0.088 \pm 0.007$	3061	83	37	-67.3	98	72	2	1.11
J1849+6705	B	2.70	$2.654 \pm 0.033$	59	$0.178 \pm 0.012$	3068	83	36	-59.1	1200	540	22	1.25
J1850+2825	A	0.22	$0.396 \pm 0.025$	65	$0.203 \pm 0.006$	2462	306	39	-12.1	194	198	10	1.08
J1922+1530	A	0.16	$0.373 \pm 0.023$	66	$0.231 \pm 0.008$	2445	435	39	-9.4	212	214	9	0.88
J1927+6117	C	0.70	$0.298 \pm 0.023$	44	$0.155 \pm 0.009$	3064	126	35	-3.9	450	199	7	0.97
J1930+1532	A	0.40	$0.433 \pm 0.029$	66	$0.143 \pm 0.009$	2454	390	39	-8.7	372	183	5	1.02
J1933+6540	C	0.13	$0.179 \pm 0.019$	46	$0.100 \pm 0.010$	3072	129	40	-2.1	105	76	3	0.97
J1939+3817	B	0.06	$0.267 \pm 0.019$	45	$0.060 \pm 0.005$	2475	146	37	-12.1	65	64	3	1.27
J1955+5131	B	0.69	$0.227 \pm 0.028$	43	$0.175 \pm 0.005$	2472	126	36	-8.3	261	156	5	1.12
J2002+1501	C	0.24	$0.340 \pm 0.029$	47	$0.243 \pm 0.018$	3020	287	43	-5.6	252	183	5	1.05
J2002+4725	B	0.23	$0.277 \pm 0.023$	44	$0.067 \pm 0.005$	2474	128	37	-11.7	98	75	3	1.03
J2007+3722	B	0.16	$0.248 \pm 0.018$	45	$0.064 \pm 0.005$	2475	149	37	-10.7	137	79	2	1.19
J2012+4628	C	0.49	$0.246 \pm 0.030$	42	$0.262 \pm 0.010$	2400	92	38	-19.3	441	279	7	1.27
J2015+3410	C	0.07	$0.175 \pm 0.015$	64	$0.067 \pm 0.006$	2410	157	46	-20.7	43	50	3	0.98
J2015+3710	B	2.86	$0.700 \pm 0.044$	36	$0.224 \pm 0.027$	30							

**Table 6.** Image Parameters *continued*

Source (J2000)	Obs (2)	$S_{86\text{GHz}}$ (3)	$S_S$ (4)	$B_S$ (5)	$S_L$ (6)	$B_L$ (7)	$B_a$ (8)	$B_b$ (9)	$B_{PA}$ (10)	$S_t$ (11)	$S_p$ (12)	$\sigma$ (13)	$\xi_r$ (14)
J2017+7440	A	0.24	$0.310 \pm 0.011$	57	$0.141 \pm 0.012$	3138	111	38	-24.7	116	105	4	0.93
J2022+6136	A	0.41	$0.287 \pm 0.023$	59	$0.132 \pm 0.008$	3138	111	38	-27.9	138	107	2	1.10
J2022+7611	A	0.82	$0.253 \pm 0.052$	56	$0.257 \pm 0.013$	3138	104	38	-31.6	767	192	6	1.46
J2024+1718	C	0.16	$0.208 \pm 0.019$	65	$0.307 \pm 0.021$	3075	255	49	-9.1	146	146	8	0.67
J2051+1743	C	0.55	$0.328 \pm 0.017$	63	$0.394 \pm 0.035$	3016	252	45	-8.4	525	362	4	0.98
J2109+3532	A	0.51	$0.495 \pm 0.033$	56	$0.176 \pm 0.008$	2474	225	37	-18.9	390	223	2	1.04
J2114+4634	A	0.07	$0.471 \pm 0.016$	55	$0.174 \pm 0.007$	3010	178	36	-35.9	304	304	4	1.09
J2137+5101	A	0.19	$0.341 \pm 0.021$	54	$0.172 \pm 0.010$	3070	141	36	-32.3	260	177	2	1.30
J2154+1727	C	0.13	$0.153 \pm 0.010$	67	$0.101 \pm 0.008$	3139	309	39	-10.7	61	62	3	0.90
J2202+4216	A	...	$3.606 \pm 0.000$	67	$0.837 \pm 0.000$	2854	165	35	-35.4	5778	1260	45	0.94
J2202+4216	C	...	$3.255 \pm 0.030$	110	$2.772 \pm 0.046$	715	2399	210	-74.6	4546	3701	64	0.70
J2203+1725	C	1.08	$1.007 \pm 0.022$	66	$0.311 \pm 0.027$	3080	351	40	-14.4	706	239	9	1.29
J2203+3145	C	1.56	$0.983 \pm 0.026$	62	$0.113 \pm 0.006$	3136	212	35	-17.1	667	167	4	1.16
J2210+2013	A	0.48	$0.523 \pm 0.026$	58	$0.212 \pm 0.016$	3042	286	38	-10.0	255	266	19	1.15
J2212+2355	A	0.34	$0.515 \pm 0.045$	58	$0.089 \pm 0.009$	2473	286	39	-12.8	127	98	4	1.06
J2217+2421	C	0.55	$0.472 \pm 0.014$	63	$0.165 \pm 0.016$	3086	270	38	-18.3	221	171	7	1.22
J2218+1520	A	0.35	$0.453 \pm 0.056$	62	$0.293 \pm 0.012$	3064	344	39	-11.2	283	222	7	0.93
J2218+1520	A	0.35	$0.453 \pm 0.056$	62	$0.293 \pm 0.012$	3064	344	39	-11.2	283	222	7	0.93
J2253+1608	A	30.38	$35.567 \pm 0.400$	58	$9.270 \pm 0.124$	2329	469	72	-15.7	21958	10166	338	1.10
J2253+1608	B	15.97	$16.897 \pm 0.269$	63	$1.061 \pm 0.075$	1770	249	88	-17.0	17324	4550	74	1.04
J2253+1608	C	5.74	$5.792 \pm 0.051$	59	$0.476 \pm 0.030$	3065	270	34	-5.0	4073	1100	21	1.03
J2305+8242	A	0.25	...	...	...	...	101	38	7.1	145	145	3	1.41
J2311+4543	A	0.36	$0.298 \pm 0.023$	62	$0.155 \pm 0.010$	3134	142	39	-26.3	235	132	2	1.13
J2312+7241	C	0.13	$0.152 \pm 0.014$	46	$0.177 \pm 0.015$	2870	112	41	-26.6	128	106	4	1.20
J2322+4445	A	0.23	$0.333 \pm 0.025$	63	$0.159 \pm 0.006$	3130	147	38	-25.9	141	123	3	1.13
J2322+5057	A	0.59	$0.391 \pm 0.030$	63	$0.151 \pm 0.007$	3130	137	40	-32.7	426	145	3	1.00
J2330+3348	C	0.22	$0.159 \pm 0.013$	60	$0.225 \pm 0.022$	3066	178	45	-16.2	154	133	5	1.03
J2354+4553	A	0.31	$0.289 \pm 0.021$	62	$0.144 \pm 0.008$	3132	155	39	-28.7	141	124	3	1.19

**Columns:** (1) – IAU Source name (J2000); (2) – observing epochs – A: October 2010; B: May 2011 and C: October 2011; (3) – total single dish flux density measured at 86 GHz obtained from the pointing and calibration scan measurements at Pico Veleta or Plateau de Bure [Jy]; (4),(6) – correlated flux densities [Jy] measured on projected baseline lengths listed in columns (5) and (7) [ $M\lambda$ ]; (8) – major axis of the restoring beam [ $\mu\text{as}$ ]; (9) – minor axis of the restoring beam [ $\mu\text{as}$ ]; (10) – position angle of the major axis [degrees]; (11) – total clean flux density [mJy]; (12) – peak flux density [mJy/beam]; (13) – off-source r.m.s noise in the residual image [mJy/beam]; (14) – quality factor of the residual noise in the image. (This table is also available in a machine-readable and Virtual Observatory (VO) forms in the online journal.)

**Table 7.** Model Fit Parameters

Source (J2000) (1)	Obs (2)	Comp (3)	$S_{\text{tot}}$ (4)	$S_{\text{peak}}$ (5)	$d$ (6)	$r$ (7)	$\theta$ (8)	$T_b$ (9)	$T_{\text{b,min}}$ (10)	$T_{\text{b,lim}}$ (11)
J0013+4051	C	1	288 ± 71	278 ± 49	<14	...	...	>28.642	4.46	9.69
J0013+4051	C	2	194 ± 61	136 ± 35	34 ± 9	41 ± 4	-30.5 ± 6.2	3.428 ± 1.647	...	...
J0017+8135	B	1	99 ± 22	69 ± 12	30 ± 5	...	...	8.115 ± 2.745	1.89	3
J0017+8135	B	2	35 ± 18	11 ± 5	77 ± 38	431 ± 19	-179.3 ± 2.5	0.435 ± 0.377	...	...
J0030+7037	B	1	121 ± 26	90 ± 16	26 ± 5	...	...	2.947 ± 0.970	1.78	2.26
J0030+7037	B	2	41 ± 45	4 ± 4	22 ± 24	53 ± 12	130.3 ± 12.7	1.395 ± 2.651	...	...
J0034+2754	C	1	72 ± 17	57 ± 10	26 ± 5	...	...	6.803 ± 2.367	3.29	4.64
J0034+2754	C	2	88 ± 36	13 ± 5	777 ± 316	758 ± 158	-49.2 ± 11.8	0.010 ± 0.007	...	...
J0034+2754	C	3	12 ± 7	14 ± 5	<41	1217 ± 8	-33.5 ± 0.4	>0.494	...	...
J0034+2754	C	4	14 ± 8	11 ± 5	59 ± 26	1713 ± 13	-30.2 ± 0.4	0.261 ± 0.221	...	...
J0034+2754	C	5	15 ± 9	10 ± 5	<37	1720 ± 9	-40.4 ± 0.3	>0.732	...	...
J0044+6803	B	1	100 ± 24	100 ± 17	<10	...	...	>16.750	1.84	2.61
J0044+6803	B	2	28 ± 14	23 ± 9	22 ± 8	65 ± 4	131.2 ± 3.6	0.972 ± 0.704	...	...
J0046+2456	A	1	199 ± 52	157 ± 32	28 ± 6	...	...	7.484 ± 2.942	4.11	6.06
J0046+2456	A	2	60 ± 31	39 ± 17	38 ± 16	171 ± 8	79.1 ± 2.7	1.225 ± 0.988	...	...
J0057+3021	A	1	298 ± 72	208 ± 41	33 ± 7	...	...	4.596 ± 1.694	9.32	23.1
J0102+5824	B	1	1030 ± 199	942 ± 134	15 ± 2	...	...	130.538 ± 36.496	8.09	24.2
J0102+5824	B	2	1633 ± 481	239 ± 70	193 ± 56	51 ± 28	92.0 ± 28.7	1.193 ± 0.604	...	...
J0102+5824	B	3	188 ± 89	166 ± 59	<18	90 ± 3	-99.6 ± 2.0	>16.293	...	...
J0109+6133	B	1	397 ± 66	231 ± 33	40 ± 6	...	...	7.221 ± 1.880	2.98	3.99
J0112+3522	A	1	201 ± 38	95 ± 16	52 ± 9	...	...	1.790 ± 0.544	2.7	3.62
J0112+3522	A	2	24 ± 12	34 ± 10	35 ± 10	182 ± 5	-110.6 ± 1.6	0.459 ± 0.300	...	...
J0113+4948	A	1	295 ± 75	235 ± 46	24 ± 5	...	...	11.840 ± 4.463	3.34	6.83
J0126+7046	B	1	82 ± 19	68 ± 12	22 ± 4	...	...	2.719 ± 0.923	0.981	1.28
J0136+4751	B	1	960 ± 166	874 ± 112	19 ± 2	...	...	82.095 ± 20.530	3.98	4.71
J0136+4751	B	2	529 ± 129	359 ± 72	41 ± 8	195 ± 4	-80.0 ± 1.2	9.473 ± 3.554	...	...
J0136+4751	B	3	172 ± 73	154 ± 49	<26	274 ± 4	-124.2 ± 0.9	>7.746	...	...
J0136+4751	B	4	121 ± 63	103 ± 41	41 ± 16	508 ± 8	-58.4 ± 0.9	2.238 ± 1.700	...	...
J0136+4751	B	5	258 ± 90	191 ± 54	31 ± 9	858 ± 4	-23.5 ± 0.3	8.051 ± 4.259	...	...
J0136+4751	C	1	742 ± 150	737 ± 105	<14	...	...	>109.137	7.68	14.5
J0136+4751	C	2	134 ± 66	138 ± 48	248 ± 85	221 ± 43	-101.3 ± 11.0	0.067 ± 0.046	...	...
J0136+4751	C	3	231 ± 92	140 ± 48	149 ± 51	892 ± 25	-8.8 ± 1.6	0.322 ± 0.202	...	...
J0136+4751	C	4	206 ± 86	133 ± 47	219 ± 77	1145 ± 39	0.9 ± 1.9	0.131 ± 0.085	...	...
J0136+4751	C	5	356 ± 125	157 ± 50	266 ± 85	1458 ± 43	-9.3 ± 1.7	0.154 ± 0.088	...	...
J0137+2145	A	1	185 ± 34	166 ± 23	22 ± 3	...	...	6.468 ± 1.715	6.47	16.8
J0137+2145	A	2	60 ± 32	14 ± 7	252 ± 131	342 ± 65	-20.4 ± 10.8	0.016 ± 0.014	...	...
J0137+2145	A	3	68 ± 31	18 ± 8	262 ± 115	719 ± 57	-28.5 ± 4.6	0.016 ± 0.013	...	...
J0154+4743	B	1	197 ± 41	169 ± 26	23 ± 4	...	...	12.993 ± 3.920	4.64	6.76
J0154+4743	B	2	30 ± 16	31 ± 12	<32	899 ± 6	-166.4 ± 0.4	>0.978	...	...
J0154+4743	B	3	36 ± 18	35 ± 13	<29	1068 ± 5	-170.8 ± 0.3	>1.424	...	...
J0205+3212	A	1	219 ± 44	162 ± 26	33 ± 5	...	...	8.355 ± 2.541	5.87	15.5
J0205+3212	A	2	147 ± 69	23 ± 11	342 ± 158	1056 ± 79	-22.2 ± 4.3	0.051 ± 0.041	...	...
J0205+3212	A	3	253 ± 130	19 ± 10	470 ± 242	1551 ± 121	-23.0 ± 4.5	0.047 ± 0.042	...	...
J0253+3217	A	1	216 ± 47	210 ± 33	<15	...	...	>30.285	6.1	15.7
J0254+2343	A	1	154 ± 39	167 ± 29	<19	...	...	>20.054	7.58	19.9
J0310+3814	B	1	224 ± 67	190 ± 43	28 ± 6	...	...	8.355 ± 3.676	3.82	5.3
J0313+4120	B	1	334 ± 74	327 ± 52	<14	...	...	>29.994	4.39	6.7
J0313+4120	B	2	145 ± 53	88 ± 28	42 ± 13	138 ± 7	-54.0 ± 2.7	1.537 ± 0.885	...	...
J0313+4120	B	3	106 ± 43	90 ± 28	<25	177 ± 4	-115.0 ± 1.3	>3.073	...	...
J0313+4120	B	4	76 ± 37	61 ± 23	<30	485 ± 6	-133.0 ± 0.7	>1.597	...	...
J0319+4130	A	1	1626 ± 245	463 ± 67	61 ± 9	...	...	7.331 ± 1.863	6.35	12.7
J0319+4130	A	2	549 ± 113	305 ± 55	41 ± 7	135 ± 4	119.6 ± 1.6	5.426 ± 1.772	...	...
J0319+4130	A	3	656 ± 171	158 ± 40	73 ± 19	200 ± 9	-176.5 ± 2.7	2.050 ± 0.907	...	...
J0319+4130	A	4	517 ± 152	125 ± 36	74 ± 21	441 ± 11	156.2 ± 1.4	1.577 ± 0.789	...	...
J0319+4130	A	5	776 ± 258	96 ± 32	230 ± 76	712 ± 38	179.3 ± 3.1	0.245 ± 0.141	...	...
J0319+4130	A	6	1869 ± 595	103 ± 33	471 ± 150	1745 ± 75	173.1 ± 2.5	0.141 ± 0.078	...	...
J0319+4130	A	7	2289 ± 654	126 ± 36	369 ± 105	2143 ± 53	175.4 ± 1.4	0.282 ± 0.139	...	...
J0319+4130	B	1	2444 ± 287	710 ± 80	152 ± 17	...	...	1.773 ± 0.351	3.74	4.18
J0319+4130	B	2	222 ± 64	208 ± 44	<20	182 ± 2	92.4 ± 0.7	>9.792	...	...
J0319+4130	B	3	190 ± 63	122 ± 34	49 ± 14	240 ± 7	-174.9 ± 1.6	1.307 ± 0.676	...	...
J0319+4130	B	4	895 ± 241	134 ± 36	362 ± 96	365 ± 48	147.3 ± 7.5	0.115 ± 0.053	...	...
J0319+4130	B	5	147 ± 53	149 ± 38	47 ± 12	415 ± 6	106.6 ± 0.8	1.101 ± 0.556	...	...
J0319+4130	B	6	191 ± 62	137 ± 36	156 ± 41	770 ± 21	-177.4 ± 1.5	0.131 ± 0.065	...	...
J0319+4130	B	7	677 ± 166	165 ± 39	259 ± 62	937 ± 31	166.0 ± 1.9	0.169 ± 0.070	...	...
J0319+4130	B	8	118 ± 52	227 ± 46	35 ± 7	1653 ± 4	-173.0 ± 0.1	1.574 ± 0.823	...	...
J0319+4130	B	9	2135 ± 604	120 ± 34	385 ± 109	1667 ± 54	170.7 ± 1.9	0.242 ± 0.119	...	...
J0319+4130	B	10	1472 ± 359	160 ± 39	432 ± 105	2065 ± 52	174.4 ± 1.5	0.133 ± 0.056	...	...
J0319+4130	B	11	918 ± 262	119 ± 34	499 ± 141	2694 ± 71	179.1 ± 1.5	0.062 ± 0.031	...	...
J0319+4130	B	12	282 ± 86	123 ± 34	349 ± 97	3088 ± 49	174.4 ± 0.9	0.039 ± 0.019	...	...
J0319+4130	B	13	306 ± 91	124 ± 34	329 ± 91	4508 ± 46	176.2 ± 0.6	0.047 ± 0.023	...	...
J0319+4130	C	1	2077 ± 264	416 ± 52	278 ± 35	...	...	0.450 ± 0.098	1.04	2.04
J0319+4130	C	2	191 ± 50	192 ± 36	<30	202 ± 3	-120.1 ± 0.8	>3.584	...	...
J0319+4130	C	3	238 ± 56	243 ± 40	<27	410 ± 2	-151.3 ± 0.3	>5.561	...	...
J0319+4130	C	4	697 ± 181	103 ± 26	339 ± 87	594 ± 43	-176.5 ± 4.2	0.102 ± 0.045	...	...

**Table 7.** Model Fit Parameters *continued*

Source (J2000) (1)	Obs (2)	Comp (3)	$S_{\text{tot}}$ (4)	$S_{\text{peak}}$ (5)	$d$ (6)	$r$ (7)	$\theta$ (8)	$T_b$ (9)	$T_{\text{b,min}}$ (10)	$T_{\text{b,lim}}$ (11)
J0319+4130	C	5	332 ± 69	216 ± 38	112 ± 19	991 ± 10	-142.9 ± 0.6	0.448 ± 0.145	...	...
J0319+4130	C	6	466 ± 93	196 ± 36	177 ± 32	1497 ± 16	163.4 ± 0.6	0.249 ± 0.081	...	...
J0319+4130	C	7	702 ± 213	76 ± 23	391 ± 118	1636 ± 59	172.0 ± 2.1	0.077 ± 0.040	...	...
J0319+4130	C	8	31 ± 22	47 ± 18	<71	1903 ± 14	-178.6 ± 0.4	>0.105	...	...
J0319+4130	C	9	274 ± 61	216 ± 38	82 ± 14	2092 ± 7	-179.3 ± 0.2	0.691 ± 0.229	...	...
J0325+2224	C	1	377 ± 96	370 ± 68	<17	...	...	>63.551	6.46	17.4
J0325+2224	C	2	140 ± 77	55 ± 28	70 ± 36	71 ± 18	97.7 ± 14.2	1.440 ± 1.314	...	...
J0325+2224	C	3	89 ± 63	37 ± 24	67 ± 44	401 ± 22	102.9 ± 3.1	1.005 ± 1.168	...	...
J0325+4655	C	1	154 ± 40	86 ± 20	55 ± 13	...	...	0.838 ± 0.350	2.09	2.76
J0325+4655	C	2	15 ± 13	17 ± 10	<40	135 ± 11	-127.4 ± 4.8	>0.155	...	...
J0333+6536	C	1	89 ± 22	62 ± 13	31 ± 6	...	...	1.564 ± 0.598	1.85	2.33
J0344+6827	A	1	100 ± 26	97 ± 18	<14	...	...	>8.345	3.6	9.37
J0344+6827	C	1	80 ± 21	63 ± 13	25 ± 5	...	...	2.148 ± 0.829	2.25	2.82
J0359+3220	A	1	159 ± 23	128 ± 14	31 ± 4	...	...	6.284 ± 1.353	4.73	11.9
J0359+3220	A	2	16 ± 8	19 ± 6	70 ± 21	321 ± 11	-139.4 ± 1.9	0.127 ± 0.081	...	...
J0359+3220	A	3	136 ± 39	21 ± 6	277 ± 79	358 ± 39	-102.3 ± 6.3	0.068 ± 0.034	...	...
J0359+5057	A	1	512 ± 188	229 ± 77	59 ± 20	...	...	6.162 ± 3.688	7.75	40.5
J0359+5057	A	2	144 ± 88	141 ± 62	<34	299 ± 7	-151.7 ± 1.4	>5.276	...	...
J0359+5057	A	3	350 ± 196	98 ± 53	85 ± 46	478 ± 23	-137.6 ± 2.8	2.010 ± 1.907	...	...
J0428+3259	A	1	103 ± 33	103 ± 23	<21	...	...	>5.429	4.09	10.3
J0512+4041	A	1	288 ± 52	222 ± 31	30 ± 4	...	...	5.373 ± 1.444	4.93	13.9
J0512+4041	A	2	53 ± 23	41 ± 14	31 ± 11	184 ± 5	50.3 ± 1.7	0.925 ± 0.603	...	...
J0512+4041	A	3	41 ± 22	25 ± 11	76 ± 35	254 ± 17	11.3 ± 3.9	0.119 ± 0.100	...	...
J0533+4822	A	1	307 ± 68	254 ± 44	27 ± 5	...	...	15.287 ± 5.038	8.36	39.3
J0533+4822	A	2	77 ± 35	80 ± 25	<25	80 ± 4	94.2 ± 2.8	>4.554	...	...
J0533+4822	A	3	65 ± 35	41 ± 19	45 ± 20	197 ± 10	37.2 ± 2.9	1.174 ± 0.984	...	...
J0533+4822	A	4	76 ± 35	67 ± 23	<25	262 ± 4	66.6 ± 0.9	>4.434	...	...
J0604+2429	A	1	247 ± 48	197 ± 30	28 ± 4	...	...	11.314 ± 3.293	4.55	14.3
J0612+4122	A	1	186 ± 24	162 ± 16	20 ± 2	...	...	7.404 ± 1.423	4.87	12.9
J0612+4122	A	2	34 ± 18	7 ± 4	281 ± 148	275 ± 74	161.5 ± 15.0	0.007 ± 0.006	...	...
J0612+4122	A	3	20 ± 12	7 ± 4	210 ± 114	687 ± 57	130.3 ± 4.8	0.008 ± 0.007	...	...
J0612+4122	A	4	37 ± 19	7 ± 4	295 ± 154	918 ± 77	167.9 ± 4.8	0.007 ± 0.006	...	...
J0612+4122	A	5	14 ± 8	8 ± 4	45 ± 22	1602 ± 11	160.2 ± 0.4	0.118 ± 0.103	...	...
J0618+4207	A	1	158 ± 28	145 ± 19	17 ± 2	...	...	9.532 ± 2.472	4.66	13.1
J0632+3200	A	1	180 ± 46	175 ± 32	<17	...	...	>28.180	3.98	12.2
J0638+5933	B	1	141 ± 33	70 ± 15	50 ± 11	...	...	0.924 ± 0.353	1.33	1.62
J0639+7324	C	1	264 ± 63	122 ± 26	52 ± 11	...	...	4.618 ± 1.782	2.04	2.57
J0639+7324	C	2	92 ± 38	45 ± 17	45 ± 17	413 ± 8	-54.0 ± 1.2	2.095 ± 1.378	...	...
J0642+8811	C	1	79 ± 22	74 ± 15	14 ± 3	...	...	6.197 ± 2.495	1.92	2.56
J0642+8811	C	2	17 ± 11	17 ± 8	57 ± 25	58 ± 13	-51.1 ± 12.3	0.086 ± 0.077	...	...
J0642+8811	C	3	25 ± 15	13 ± 7	57 ± 30	675 ± 15	-51.1 ± 1.3	0.124 ± 0.119	...	...
J0650+6001	B	1	162 ± 41	74 ± 17	50 ± 12	...	...	1.567 ± 0.654	1.78	2.48
J0700+1709	A	1	444 ± 86	214 ± 37	19 ± 3	...	...	19.284 ± 6.029	3.67	9.79
J0700+1709	A	2	211 ± 62	95 ± 25	51 ± 14	185 ± 7	-121.2 ± 2.1	1.325 ± 0.631	...	...
J0707+6110	B	1	113 ± 22	81 ± 13	29 ± 5	...	...	2.253 ± 0.672	2.08	2.85
J0707+6110	B	2	54 ± 16	91 ± 14	57 ± 8	52 ± 4	-122.0 ± 4.7	0.280 ± 0.101	...	...
J0713+1935	A	1	210 ± 65	216 ± 47	<26	...	...	>7.664	4.69	15.7
J0721+7120	B	1	1489 ± 275	1269 ± 178	18 ± 3	...	...	97.111 ± 26.362	20.5	204
J0721+7120	B	2	578 ± 178	416 ± 104	27 ± 7	44 ± 3	10.9 ± 4.4	17.093 ± 8.027	...	...
J0721+7120	B	3	594 ± 179	445 ± 108	25 ± 6	111 ± 3	32.1 ± 1.6	20.395 ± 9.295	...	...
J0721+7120	B	4	357 ± 175	139 ± 63	50 ± 23	276 ± 11	41.7 ± 2.3	3.120 ± 2.529	...	...
J0721+7120	C	1	1006 ± 211	984 ± 147	<3	...	...	>372.818	...	...
J0733+5022	C	1	148 ± 35	112 ± 21	32 ± 6	...	...	4.095 ± 1.450	1.52	2.39
J0741+3112	C	1	295 ± 63	266 ± 42	19 ± 3	...	...	21.114 ± 6.562	11.5	28.8
J0741+3112	C	2	68 ± 33	50 ± 19	44 ± 17	860 ± 8	153.7 ± 0.6	0.958 ± 0.698	...	...
J0741+3112	C	3	76 ± 38	39 ± 17	204 ± 91	1285 ± 46	145.4 ± 2.0	0.049 ± 0.039	...	...
J0747+7639	B	1	63 ± 17	59 ± 12	<13	...	...	>6.085	1.53	1.94
J0748+2400	C	1	522 ± 112	376 ± 66	36 ± 6	...	...	9.578 ± 3.142	10.7	24.3
J0748+2400	C	2	253 ± 98	94 ± 34	88 ± 32	181 ± 16	-68.5 ± 5.0	0.762 ± 0.491	...	...
J0748+2400	C	3	136 ± 71	58 ± 28	74 ± 36	486 ± 18	-72.0 ± 2.1	0.573 ± 0.490	...	...
J0753+5352	C	1	339 ± 75	335 ± 53	<11	...	...	>52.682	9.99	20.6
J0753+5352	C	2	72 ± 40	42 ± 20	58 ± 28	158 ± 14	-21.0 ± 5.1	0.420 ± 0.370	...	...
J0753+5352	C	3	88 ± 52	34 ± 18	88 ± 48	587 ± 24	-37.5 ± 2.4	0.225 ± 0.219	...	...
J0808+4052	C	1	311 ± 50	223 ± 29	32 ± 4	...	...	12.373 ± 3.022	7.3	21
J0808+4052	C	2	55 ± 27	21 ± 10	79 ± 36	1038 ± 18	152.2 ± 1.0	0.349 ± 0.281	...	...
J0809+5341	C	1	95 ± 30	92 ± 21	<17	...	...	>17.779	3.81	5.12
J0814+6431	C	1	352 ± 59	318 ± 39	19 ± 2	...	...	15.909 ± 3.835	8.29	22.3
J0815+3635	C	1	399 ± 75	364 ± 50	19 ± 3	...	...	36.653 ± 9.938	11.8	31.3
J0817+3227	C	1	416 ± 71	372 ± 47	26 ± 3	...	...	10.075 ± 2.482	11.4	28.1
J0817+3227	C	2	30 ± 21	28 ± 14	67 ± 34	1295 ± 17	17.2 ± 0.7	0.111 ± 0.110	...	...
J0817+3227	C	3	33 ± 21	35 ± 15	<44	2385 ± 10	13.5 ± 0.2	>0.278	...	...
J0824+3916	C	1	257 ± 37	230 ± 25	18 ± 2	...	...	30.060 ± 6.343	7.62	19.5
J0824+3916	C	2	66 ± 28	18 ± 7	157 ± 65	1048 ± 32	-23.0 ± 1.8	0.097 ± 0.070	...	...
J0854+2006	B	1	1253 ± 390	1250 ± 275	<25	...	...	>41.703	14.6	61.6

**Table 7.** Model Fit Parameters *continued*

Source (J2000) (1)	Obs (2)	Comp (3)	$S_{\text{tot}}$ (4)	$S_{\text{peak}}$ (5)	$d$ (6)	$r$ (7)	$\theta$ (8)	$T_b$ (9)	$T_{\text{b,min}}$ (10)	$T_{\text{b,lim}}$ (11)
J0854+2006	B	2	2714 ± 774	835 ± 228	72 ± 20	260 ± 10	-25.1 ± 2.2	11.299 ± 5.419	...	...
J0909+4253	A	1	160 ± 27	152 ± 19	13 ± 2	...	...	27.793 ± 6.776	5.16	14.3
J0909+4253	A	2	31 ± 13	26 ± 8	26 ± 8	92 ± 4	-157.0 ± 2.5	1.242 ± 0.742	...	...
J0917+6530	C	1	189 ± 77	187 ± 54	<20	...	...	>8.098	8.31	22.3
J0920+4441	A	1	485 ± 106	405 ± 68	24 ± 4	...	...	45.793 ± 14.769	6.54	25.1
J0920+4441	A	2	206 ± 71	163 ± 44	28 ± 8	179 ± 4	-126.5 ± 1.2	13.987 ± 7.190	...	...
J0920+4441	A	3	116 ± 62	57 ± 28	58 ± 28	378 ± 14	-132.8 ± 2.1	1.818 ± 1.576	...	...
J0925+3612	A	1	170 ± 38	207 ± 29	20 ± 3	...	...	14.737 ± 4.375	5.51	14.3
J0927+3902	C	1	355 ± 65	332 ± 45	18 ± 2	...	...	30.384 ± 8.039	22	69.8
J0927+3902	C	2	175 ± 46	193 ± 34	<18	53 ± 2	-44.1 ± 1.7	>15.730	...	...
J0927+3902	C	3	913 ± 217	111 ± 26	308 ± 73	181 ± 36	-149.5 ± 11.4	0.269 ± 0.110	...	...
J0927+3902	C	4	757 ± 173	122 ± 27	220 ± 50	203 ± 25	-20.0 ± 6.9	0.437 ± 0.171	...	...
J0927+3902	C	5	338 ± 114	58 ± 19	274 ± 91	1898 ± 46	-66.2 ± 1.4	0.126 ± 0.073	...	...
J0937+5008	C	1	320 ± 85	320 ± 60	<15	...	...	>31.266	10.7	31.4
J0945+3534	A	1	168 ± 35	155 ± 24	21 ± 3	...	...	14.028 ± 4.255	6.22	15.8
J0956+2515	A	1	476 ± 97	370 ± 59	26 ± 4	...	...	19.912 ± 6.067	6.43	15
J0956+2515	A	2	243 ± 76	129 ± 36	45 ± 12	181 ± 6	-118.8 ± 2.0	3.457 ± 1.742	...	...
J0956+2515	A	3	73 ± 44	42 ± 22	52 ± 27	330 ± 14	-129.8 ± 2.4	0.766 ± 0.730	...	...
J0957+5522	C	1	229 ± 74	231 ± 52	<16	...	...	>26.656	10.3	29.4
J0958+4725	C	1	310 ± 56	244 ± 35	29 ± 4	...	...	17.992 ± 4.847	8.62	20.6
J1013+2449	A	1	225 ± 48	185 ± 30	23 ± 4	...	...	19.153 ± 5.999	8.4	21.2
J1018+3542	C	1	393 ± 81	380 ± 56	<12	...	...	>93.102	10	26.1
J1018+3542	C	2	55 ± 32	47 ± 21	<32	535 ± 7	164.1 ± 0.8	>1.927	...	...
J1033+4116	C	1	542 ± 80	290 ± 38	44 ± 6	...	...	9.775 ± 2.315	8.88	22.8
J1033+4116	C	2	162 ± 66	36 ± 14	183 ± 72	482 ± 36	23.3 ± 4.3	0.168 ± 0.116	...	...
J1033+6051	C	1	332 ± 55	290 ± 36	12 ± 2	...	...	88.683 ± 21.429	6.23	20.1
J1033+6051	C	2	118 ± 49	31 ± 13	72 ± 29	93 ± 14	-133.4 ± 8.8	0.902 ± 0.636	...	...
J1033+6051	C	3	108 ± 52	24 ± 11	64 ± 30	627 ± 15	-171.6 ± 1.4	1.059 ± 0.862	...	...
J1033+6051	C	4	146 ± 72	22 ± 11	228 ± 112	1333 ± 56	176.9 ± 2.4	0.111 ± 0.095	...	...
J1038+4244	C	1	180 ± 47	184 ± 34	<15	...	...	>16.790	7.8	19.5
J1043+2408	A	1	576 ± 141	410 ± 82	32 ± 6	...	...	14.419 ± 5.392	7.8	16.5
J1043+2408	A	2	245 ± 97	152 ± 51	37 ± 12	256 ± 6	73.3 ± 1.4	4.644 ± 2.886	...	...
J1044+8054	B	1	633 ± 101	192 ± 29	56 ± 8	...	...	7.563 ± 2.022	2.41	4.08
J1044+8054	B	2	130 ± 40	61 ± 17	45 ± 12	260 ± 6	13.8 ± 1.4	2.372 ± 1.173	...	...
J1045+1735	A	1	280 ± 58	225 ± 36	28 ± 5	...	...	11.178 ± 3.422	9.1	20.5
J1058+8114	B	1	328 ± 62	245 ± 37	26 ± 4	...	...	13.225 ± 3.756	3.72	7.47
J1058+8114	B	2	187 ± 55	78 ± 21	48 ± 13	158 ± 7	-163.2 ± 2.4	2.236 ± 1.086	...	...
J1058+8114	B	3	52 ± 26	38 ± 15	24 ± 10	804 ± 5	177.0 ± 0.3	2.480 ± 1.874	...	...
J1103+3014	B	1	342 ± 65	227 ± 36	42 ± 7	...	...	4.386 ± 1.281	2.59	6.7
J1103+3014	B	2	125 ± 40	82 ± 22	46 ± 12	114 ± 6	129.9 ± 3.1	1.341 ± 0.663	...	...
J1130+3815	B	1	371 ± 75	275 ± 45	33 ± 5	...	...	15.450 ± 4.721	3.2	11.3
J1130+3815	B	2	409 ± 93	167 ± 35	79 ± 16	126 ± 8	-20.2 ± 3.8	2.985 ± 1.115	...	...
J1146+3958	B	1	1286 ± 244	677 ± 114	46 ± 8	...	...	20.540 ± 6.245	8.07	61.3
J1146+3958	B	2	202 ± 91	196 ± 63	<31	273 ± 5	-80.3 ± 1.0	>7.391	...	...
J1152+4939	B	1	106 ± 32	74 ± 18	32 ± 8	...	...	3.458 ± 1.580	0.955	1.38
J1153+4931	B	1	1085 ± 297	1040 ± 205	<17	...	...	>80.801	9.56	110
J1153+4931	B	2	439 ± 210	269 ± 110	42 ± 17	484 ± 9	176.9 ± 1.0	5.360 ± 4.019	...	...
J1153+8058	B	1	125 ± 23	75 ± 12	42 ± 7	...	...	2.702 ± 0.786	1.41	1.76
J1200+5300	C	1	102 ± 25	78 ± 15	32 ± 6	...	...	5.006 ± 1.833	3.55	4.74
J1203+4803	C	1	149 ± 35	81 ± 17	47 ± 10	...	...	2.024 ± 0.765	3.26	4.37
J1219+6344	C	1	71 ± 28	66 ± 19	<23	...	...	>2.232	3.04	4.02
J1224+2122	A	1	408 ± 121	383 ± 83	<33	...	...	>8.697	8.58	23
J1224+2122	A	2	1434 ± 512	152 ± 54	614 ± 218	69 ± 109	27.8 ± 57.8	0.090 ± 0.055	...	...
J1229+0203	A	1	3108 ± 713	1800 ± 357	202 ± 40	...	...	1.456 ± 0.528	2.21	5.32
J1229+0203	A	2	1641 ± 517	1020 ± 273	170 ± 46	671 ± 23	-139.2 ± 1.9	1.079 ± 0.531	...	...
J1229+0203	A	3	261 ± 240	158 ± 124	157 ± 123	1391 ± 62	-138.1 ± 2.5	0.203 ± 0.294	...	...
J1229+0203	A	4	401 ± 254	384 ± 176	<103	1849 ± 24	-118.8 ± 0.7	>0.722	...	...
J1229+0203	B	1	2804 ± 722	1590 ± 356	219 ± 49	...	...	1.122 ± 0.458	0.188	0.622
J1241+5458	C	1	67 ± 22	65 ± 16	<19	...	...	>3.108	2.59	3.47
J1256-0547	B	1	10005 ± 2157	6440 ± 1167	105 ± 19	...	...	23.196 ± 7.770	11.8	61.4
J1256-0547	B	2	2825 ± 1149	2130 ± 692	80 ± 26	214 ± 13	-21.0 ± 3.5	11.097 ± 6.811	...	...
J1256-0547	B	3	8880 ± 3002	2080 ± 685	370 ± 122	308 ± 61	-152.6 ± 11.2	1.644 ± 0.946	...	...
J1256-0547	B	4	1470 ± 911	902 ± 476	203 ± 107	838 ± 54	-107.6 ± 3.7	0.905 ± 0.878	...	...
J1259+5140	C	1	172 ± 51	138 ± 32	27 ± 6	...	...	3.826 ± 1.689	3.78	5.96
J1259+5140	C	2	25 ± 21	29 ± 16	<37	72 ± 10	-144.5 ± 8.2	>0.291	...	...
J1306+5529	C	1	70 ± 21	57 ± 13	29 ± 7	...	...	3.505 ± 1.540	1.01	1.41
J1310+3220	B	1	381 ± 89	225 ± 45	38 ± 8	...	...	8.573 ± 3.143	4.35	8.99
J1310+3220	B	2	166 ± 60	98 ± 30	38 ± 12	147 ± 6	-97.0 ± 2.3	3.718 ± 2.114	...	...
J1310+3220	B	3	82 ± 44	47 ± 22	34 ± 16	275 ± 8	-63.2 ± 1.7	2.317 ± 1.973	...	...
J1310+3220	B	4	368 ± 165	52 ± 23	391 ± 174	491 ± 87	-67.1 ± 10.0	0.079 ± 0.061	...	...
J1327+2210	A	1	365 ± 63	288 ± 39	29 ± 4	...	...	17.640 ± 4.570	7.28	21.4
J1329+3154	A	1	217 ± 41	197 ± 28	19 ± 3	...	...	13.054 ± 3.608	7.55	27.4
J1329+3154	A	2	26 ± 15	36 ± 12	<35	107 ± 6	-35.7 ± 3.3	>0.460	...	...
J1329+3154	A	3	12 ± 11	21 ± 10	<50	154 ± 12	-174.2 ± 4.4	>0.108	...	...

**Table 7.** Model Fit Parameters *continued*

Source (J2000) (1)	Obs (2)	Comp (3)	$S_{\text{tot}}$ (4)	$S_{\text{peak}}$ (5)	$d$ (6)	$r$ (7)	$\theta$ (8)	$T_b$ (9)	$T_{\text{b,min}}$ (10)	$T_{\text{b,lim}}$ (11)
J1341+2816	A	1	233 ± 54	194 ± 35	24 ± 4	...	...	15.200 ± 5.217	9.39	29.7
J1353+7532	B	1	98 ± 20	64 ± 11	34 ± 6	...	...	3.626 ± 1.130	1.79	2.24
J1357+7643	B	1	211 ± 41	174 ± 26	21 ± 3	...	...	19.653 ± 5.601	2.3	3.79
J1407+2827	A	1	222 ± 46	191 ± 30	23 ± 4	...	...	7.190 ± 2.163	8.47	25.3
J1407+2827	A	2	102 ± 45	30 ± 12	261 ± 109	551 ± 55	-23.1 ± 5.7	0.027 ± 0.020	...	...
J1419+3821	A	1	274 ± 72	136 ± 32	49 ± 11	...	...	5.429 ± 2.287	4.6	6.03
J1506+4239	A	1	270 ± 68	191 ± 39	31 ± 6	...	...	7.359 ± 2.833	2.62	3.28
J1506+8319	B	1	86 ± 19	65 ± 11	27 ± 5	...	...	6.953 ± 2.301	2.01	2.69
J1521+4336	A	1	204 ± 62	202 ± 44	<17	...	...	>37.360	4.23	10.4
J1549+5038	C	1	311 ± 56	221 ± 32	30 ± 4	...	...	18.257 ± 4.997	4.35	11.5
J1549+5038	C	2	32 ± 18	39 ± 14	<40	377 ± 7	-159.8 ± 1.1	>1.055	...	...
J1608+4012	B	1	308 ± 83	305 ± 59	<17	...	...	>27.882	4.04	7.66
J1624+5741	C	1	336 ± 58	226 ± 32	35 ± 5	...	...	8.000 ± 2.130	4.88	12.9
J1635+3808	C	1	1562 ± 290	1000 ± 156	38 ± 6	...	...	51.152 ± 14.756	8.16	44.6
J1637+4717	B	1	748 ± 109	367 ± 48	45 ± 6	...	...	10.609 ± 2.509	4.14	7.63
J1640+3946	B	1	400 ± 67	196 ± 29	46 ± 7	...	...	8.451 ± 2.285	4.45	6.38
J1640+3946	B	2	226 ± 53	96 ± 21	50 ± 11	137 ± 5	158.0 ± 2.3	3.991 ± 1.547	...	...
J1640+3946	B	3	87 ± 40	26 ± 12	49 ± 22	261 ± 11	-110.7 ± 2.4	1.570 ± 1.208	...	...
J1640+3946	B	4	143 ± 52	40 ± 14	193 ± 67	261 ± 34	-62.3 ± 7.3	0.168 ± 0.103	...	...
J1642+3948	A	1	770 ± 234	396 ± 107	44 ± 12	...	...	10.535 ± 5.142	5.15	11.2
J1642+3948	A	2	975 ± 374	217 ± 81	182 ± 68	198 ± 34	-109.3 ± 9.8	0.774 ± 0.506	...	...
J1642+3948	A	3	339 ± 176	141 ± 67	37 ± 18	67 ± 9	-65.4 ± 7.5	6.571 ± 5.598	...	...
J1642+3948	A	4	403 ± 215	127 ± 65	73 ± 37	723 ± 19	-131.1 ± 1.5	1.973 ± 1.763	...	...
J1642+3948	B	1	1090 ± 205	395 ± 70	55 ± 10	...	...	9.413 ± 2.952	5.48	11.5
J1642+3948	B	2	1005 ± 258	201 ± 51	127 ± 32	176 ± 16	-105.2 ± 5.2	1.628 ± 0.715	...	...
J1642+3948	B	3	630 ± 234	100 ± 37	257 ± 94	807 ± 47	-109.2 ± 3.3	0.251 ± 0.160	...	...
J1642+3948	B	4	181 ± 74	109 ± 38	66 ± 23	1524 ± 12	-109.4 ± 0.4	1.079 ± 0.693	...	...
J1646+4059	B	1	74 ± 18	64 ± 12	22 ± 4	...	...	4.754 ± 1.733	2.9	3.9
J1646+4059	B	2	8 ± 7	10 ± 5	<46	172 ± 12	-34.1 ± 4.1	>0.112	...	...
J1653+3107	A	1	179 ± 23	170 ± 16	16 ± 2	...	...	25.498 ± 4.702	2.5	8.79
J1653+3107	A	2	54 ± 14	27 ± 6	81 ± 19	388 ± 10	20.4 ± 1.4	0.313 ± 0.135	...	...
J1653+3107	A	3	63 ± 16	30 ± 7	105 ± 24	1067 ± 12	-18.5 ± 0.6	0.215 ± 0.087	...	...
J1659+2629	A	1	197 ± 25	175 ± 16	22 ± 2	...	...	11.971 ± 2.181	2.48	8.81
J1659+2629	A	2	66 ± 16	32 ± 7	70 ± 15	342 ± 8	23.2 ± 1.3	0.403 ± 0.161	...	...
J1659+2629	A	3	65 ± 15	37 ± 8	64 ± 13	1099 ± 7	0.2 ± 0.3	0.474 ± 0.178	...	...
J1701+3954	A	1	155 ± 27	156 ± 19	<11	...	...	>31.997	2.5	7.98
J1701+3954	A	2	54 ± 17	32 ± 9	52 ± 14	416 ± 7	-139.3 ± 1.0	0.493 ± 0.249	...	...
J1701+3954	A	3	52 ± 22	16 ± 6	179 ± 73	426 ± 37	-167.6 ± 4.9	0.040 ± 0.029	...	...
J1716+6836	C	1	273 ± 75	217 ± 47	26 ± 6	...	...	11.847 ± 4.866	14.7	39
J1726+3213	A	1	174 ± 42	177 ± 30	<17	...	...	>19.597	3.41	11.6
J1735+5049	A	1	148 ± 22	148 ± 16	<9	...	...	>54.376	2.51	8.01
J1735+5049	A	2	19 ± 9	11 ± 4	98 ± 41	286 ± 21	-25.2 ± 4.1	0.060 ± 0.045	...	...
J1735+5049	A	3	12 ± 7	11 ± 5	37 ± 15	301 ± 7	31.1 ± 1.4	0.279 ± 0.221	...	...
J1735+5049	A	4	29 ± 11	16 ± 5	109 ± 37	915 ± 18	-3.6 ± 1.2	0.075 ± 0.046	...	...
J1735+5049	A	5	33 ± 12	20 ± 6	108 ± 32	1047 ± 16	-19.5 ± 0.9	0.087 ± 0.047	...	...
J1746+6226	B	1	91 ± 21	69 ± 13	30 ± 6	...	...	8.032 ± 2.812	2.08	2.79
J1751+2920	A	1	350 ± 72	241 ± 41	35 ± 6	...	...	4.674 ± 1.481	2.64	7.44
J1753+2848	A	1	222 ± 57	152 ± 32	34 ± 7	...	...	6.785 ± 2.663	2.69	5.76
J1800+3848	A	1	202 ± 52	197 ± 36	<18	...	...	>32.519	3.43	11.8
J1800+7828	C	1	1102 ± 184	480 ± 73	47 ± 7	...	...	13.960 ± 3.816	7.42	23.7
J1800+7828	C	2	213 ± 87	87 ± 33	51 ± 19	263 ± 10	140.0 ± 2.1	2.316 ± 1.551	...	...
J1800+7828	C	3	336 ± 122	101 ± 35	67 ± 23	966 ± 12	-118.0 ± 0.7	2.072 ± 1.266	...	...
J1808+4542	C	1	172 ± 56	182 ± 41	<31	...	...	>5.560	4.42	12
J1811+1704	A	1	361 ± 76	251 ± 44	34 ± 6	...	...	5.065 ± 1.638	10.3	36.1
J1811+1704	A	2	33 ± 24	42 ± 19	<60	65 ± 14	71.9 ± 11.9	>0.148	...	...
J1821+6818	B	1	157 ± 36	140 ± 24	19 ± 3	...	...	20.232 ± 6.774	2.13	2.79
J1821+6818	B	2	41 ± 19	40 ± 13	<19	181 ± 3	-153.4 ± 1.0	>4.929	...	...
J1821+6818	C	1	180 ± 39	168 ± 27	15 ± 2	...	...	36.726 ± 11.548	2.13	2.79
J1821+6818	C	2	34 ± 20	20 ± 10	52 ± 26	108 ± 13	-161.2 ± 7.0	0.567 ± 0.527	...	...
J1821+6818	C	3	30 ± 18	19 ± 10	42 ± 22	824 ± 11	-164.3 ± 0.8	0.767 ± 0.734	...	...
J1823+6857	B	1	77 ± 18	70 ± 12	18 ± 3	...	...	4.065 ± 1.381	2.5	3.25
J1823+6857	B	2	12 ± 8	14 ± 6	<25	41 ± 5	-141.6 ± 7.1	>0.328	...	...
J1849+6705	B	1	686 ± 185	472 ± 105	30 ± 7	...	...	21.367 ± 8.852	3.02	4.98
J1849+6705	B	2	312 ± 135	179 ± 67	35 ± 13	85 ± 7	-142.0 ± 4.4	6.905 ± 4.712	...	...
J1849+6705	B	3	213 ± 105	168 ± 65	25 ± 10	165 ± 5	-139.9 ± 1.7	9.577 ± 7.066	...	...
J1850+2825	A	1	202 ± 64	199 ± 45	<27	...	...	>16.705	3.98	21.5
J1922+1530	A	1	208 ± 64	215 ± 46	<31	...	...	>3.581	3.61	16.7
J1927+6117	C	1	449 ± 116	125 ± 31	74 ± 18	...	...	1.987 ± 0.866	2.7	3.76
J1930+1532	A	1	240 ± 50	174 ± 29	33 ± 6	...	...	3.666 ± 1.159	2.69	6.51
J1930+1532	A	2	65 ± 26	56 ± 17	<37	252 ± 6	-98.6 ± 1.3	>0.785	...	...
J1933+6540	C	1	110 ± 26	73 ± 14	39 ± 8	...	...	3.255 ± 1.192	2.61	4.63
J1939+3817	B	1	73 ± 21	64 ± 14	24 ± 5	...	...	2.180 ± 0.915	0.865	1.1
J1955+5131	B	1	228 ± 51	156 ± 29	33 ± 6	...	...	7.819 ± 2.689	1.83	4.29
J1955+5131	B	2	101 ± 47	30 ± 13	70 ± 31	514 ± 16	-23.6 ± 1.7	0.751 ± 0.590	...	...

**Table 7.** Model Fit Parameters *continued*

Source (J2000) (1)	Obs (2)	Comp (3)	$S_{\text{tot}}$ (4)	$S_{\text{peak}}$ (5)	$d$ (6)	$r$ (7)	$\theta$ (8)	$T_b$ (9)	$T_{\text{b,min}}$ (10)	$T_{\text{b,lim}}$ (11)
J2002+1501	C	1	227 ± 48	180 ± 30	33 ± 5	...	...	3.539 ± 1.119	8.55	12.2
J2002+4725	B	1	99 ± 24	74 ± 14	32 ± 6	...	...	5.296 ± 1.958	1.01	1.42
J2002+4725	B	2	29 ± 15	15 ± 7	54 ± 26	331 ± 13	106.9 ± 2.2	0.525 ± 0.449	...	...
J2007+3722	B	1	130 ± 28	59 ± 11	51 ± 10	...	...	0.829 ± 0.288	0.899	1.19
J2007+3722	B	2	22 ± 12	11 ± 5	61 ± 30	152 ± 15	117.9 ± 5.7	0.098 ± 0.088	...	...
J2012+4628	C	1	405 ± 80	274 ± 45	34 ± 6	...	...	5.638 ± 1.709	4.02	11.1
J2015+3410	C	1	46 ± 17	50 ± 13	<25	...	...	>1.227	0.864	1.08
J2015+3710	B	1	812 ± 203	789 ± 142	<14	...	...	>126.682	7.26	9.47
J2015+3710	B	2	1095 ± 420	195 ± 74	202 ± 76	102 ± 38	-117.3 ± 20.4	0.826 ± 0.544	...	...
J2015+3710	B	3	295 ± 154	128 ± 61	184 ± 88	349 ± 44	-129.6 ± 7.2	0.267 ± 0.229	...	...
J2015+3710	C	1	2622 ± 430	1890 ± 252	34 ± 4	...	...	70.539 ± 17.620	33.4	347
J2015+3710	C	2	390 ± 167	378 ± 116	<25	172 ± 4	-119.6 ± 1.3	>18.795	...	...
J2016+1632	C	1	231 ± 49	191 ± 31	31 ± 5	...	...	4.003 ± 1.257	8.95	17.2
J2016+1632	C	2	60 ± 32	25 ± 12	206 ± 102	611 ± 51	-75.6 ± 4.8	0.023 ± 0.020	...	...
J2016+3600	A	1	256 ± 42	225 ± 27	21 ± 3	...	...	9.932 ± 2.356	3.23	14.1
J2016+3600	A	2	76 ± 33	23 ± 9	148 ± 61	1222 ± 30	-35.5 ± 1.4	0.057 ± 0.041	...	...
J2017+7440	A	1	115 ± 29	104 ± 20	16 ± 3	...	...	23.727 ± 8.704	4.1	10.8
J2022+6136	A	1	120 ± 23	109 ± 16	17 ± 3	...	...	8.008 ± 2.263	4	10.6
J2022+6136	A	2	16 ± 9	21 ± 7	<26	83 ± 4	35.6 ± 3.1	>0.487	...	...
J2022+7611	A	1	226 ± 51	180 ± 32	26 ± 5	...	...	8.991 ± 3.051	6.78	27.6
J2022+7611	A	2	87 ± 39	38 ± 16	86 ± 35	105 ± 17	-51.2 ± 9.4	0.312 ± 0.227	...	...
J2022+7611	A	3	91 ± 34	63 ± 19	35 ± 11	170 ± 5	-127.7 ± 1.8	1.952 ± 1.125	...	...
J2022+7611	A	4	265 ± 94	50 ± 18	219 ± 76	338 ± 38	-122.3 ± 6.5	0.146 ± 0.089	...	...
J2024+1718	C	1	141 ± 50	146 ± 36	<31	...	...	>5.061	9.85	19.4
J2051+1743	C	1	474 ± 64	357 ± 39	39 ± 4	...	...	6.112 ± 1.251	12.6	24.5
J2051+1743	C	2	56 ± 24	37 ± 13	43 ± 15	330 ± 8	-95.0 ± 1.3	0.610 ± 0.399	...	...
J2109+3532	A	1	277 ± 30	211 ± 18	30 ± 3	...	...	6.235 ± 1.003	3.1	13
J2109+3532	A	2	29 ± 10	21 ± 6	36 ± 10	199 ± 5	127.0 ± 1.4	0.451 ± 0.237	...	...
J2109+3532	A	3	52 ± 14	28 ± 7	51 ± 12	476 ± 6	-161.0 ± 0.7	0.401 ± 0.174	...	...
J2109+3532	A	4	17 ± 8	12 ± 5	117 ± 44	1688 ± 22	-147.3 ± 0.7	0.025 ± 0.017	...	...
J2114+4634	A	1	230 ± 42	188 ± 27	21 ± 3	...	...	8.274 ± 2.253	4.37	18.3
J2137+5101	A	1	187 ± 29	173 ± 20	13 ± 1	...	...	19.666 ± 4.388	4.34	13.9
J2137+5101	A	2	27 ± 12	20 ± 7	28 ± 10	1273 ± 5	-11.9 ± 0.2	0.581 ± 0.383	...	...
J2137+5101	A	3	17 ± 9	16 ± 6	<28	1444 ± 6	-10.6 ± 0.2	>0.350	...	...
J2154+1727	C	1	69 ± 21	62 ± 14	<25	...	...	>3.690	3.78	5.05
J2202+4216	A	1	3151 ± 844	699 ± 183	89 ± 23	...	...	7.044 ± 3.216	...	...
J2202+4216	A	2	862 ± 287	785 ± 193	<19	390 ± 2	160.8 ± 0.4	>40.351	...	...
J2202+4216	A	3	792 ± 314	397 ± 141	41 ± 14	571 ± 7	168.4 ± 0.7	8.472 ± 5.419	...	...
J2202+4216	A	4	937 ± 343	456 ± 150	57 ± 19	577 ± 9	173.6 ± 0.9	5.102 ± 3.018	...	...
J2202+4216	A	5	512 ± 233	371 ± 137	28 ± 10	711 ± 5	159.4 ± 0.4	11.745 ± 8.121	...	...
J2202+4216	C	1	3364 ± 664	3280 ± 464	<110	...	...	>4.877	3.95	7.52
J2203+1725	C	1	276 ± 73	224 ± 46	40 ± 8	...	...	5.810 ± 2.296	4.77	6.4
J2203+1725	C	2	459 ± 172	75 ± 28	254 ± 94	93 ± 47	36.0 ± 26.9	0.244 ± 0.157	...	...
J2203+3145	C	1	406 ± 73	132 ± 23	66 ± 11	...	...	2.004 ± 0.608	2.42	3.5
J2203+3145	C	2	140 ± 43	48 ± 14	66 ± 19	214 ± 10	-144.1 ± 2.6	0.681 ± 0.351	...	...
J2203+3145	C	3	95 ± 31	48 ± 14	50 ± 15	223 ± 7	-12.3 ± 1.9	0.816 ± 0.432	...	...
J2210+2013	A	1	301 ± 112	268 ± 74	<29	...	162.8 ± 0.0	>7.395	3.45	7.49
J2212+2355	A	1	150 ± 38	95 ± 21	41 ± 9	...	...	3.087 ± 1.231	2.36	3.52
J2212+2355	A	2	52 ± 25	29 ± 12	41 ± 17	158 ± 8	-131.0 ± 3.1	1.081 ± 0.812	...	...
J2217+2421	C	1	252 ± 61	172 ± 34	37 ± 7	...	...	4.553 ± 1.682	3.64	5.13
J2218+1520	A	1	243 ± 60	214 ± 40	<22	...	...	>26.940	7.63	30.8
J2218+1520	A	2	22 ± 20	35 ± 17	<70	62 ± 17	-109.2 ± 15.4	>0.245	...	...
J2253+1608	A	1	23016 ± 4721	9805 ± 1850	233 ± 44	...	...	13.026 ± 4.384	147	2240
J2253+1608	A	2	10128 ± 3065	4842 ± 1322	221 ± 60	293 ± 30	-81.1 ± 5.9	6.388 ± 3.134	...	...
J2253+1608	B	1	5857 ± 977	3960 ± 547	94 ± 13	...	...	20.169 ± 5.182	8.09	27.4
J2253+1608	B	2	4871 ± 1213	1360 ± 326	264 ± 63	159 ± 32	-102.4 ± 11.3	2.135 ± 0.899	...	...
J2253+1608	B	3	614 ± 331	466 ± 200	90 ± 39	324 ± 19	-84.2 ± 3.4	2.341 ± 1.902	...	...
J2253+1608	B	4	1038 ± 533	382 ± 184	242 ± 116	445 ± 58	-63.2 ± 7.5	0.545 ± 0.465	...	...
J2253+1608	B	5	1185 ± 467	723 ± 243	118 ± 40	511 ± 20	-86.7 ± 2.2	2.613 ± 1.615	...	...
J2253+1608	B	6	861 ± 429	441 ± 196	185 ± 82	868 ± 41	-53.9 ± 2.7	0.774 ± 0.620	...	...
J2253+1608	B	7	2326 ± 856	658 ± 233	304 ± 108	945 ± 54	-36.1 ± 3.3	0.771 ± 0.480	...	...
J2253+1608	B	8	548 ± 315	416 ± 191	72 ± 33	995 ± 17	-75.4 ± 1.0	3.236 ± 2.807	...	...
J2253+1608	B	9	608 ± 377	300 ± 167	285 ± 159	1380 ± 79	-70.0 ± 3.3	0.229 ± 0.228	...	...
J2253+1608	C	1	976 ± 207	839 ± 135	19 ± 3	...	...	80.266 ± 24.921	12.5	26.9
J2253+1608	C	2	1795 ± 722	150 ± 60	327 ± 131	56 ± 65	-97.9 ± 49.2	0.515 ± 0.358	...	...
J2253+1608	C	3	587 ± 284	111 ± 53	174 ± 83	377 ± 41	-62.2 ± 6.3	0.593 ± 0.492	...	...
J2253+1608	C	4	699 ± 270	168 ± 63	70 ± 26	473 ± 13	-79.1 ± 1.6	4.349 ± 2.860	...	...
J2253+1608	C	5	456 ± 227	107 ± 52	92 ± 45	582 ± 22	-101.2 ± 2.2	1.641 ± 1.394	...	...
J2305+8242	A	1	145 ± 29	145 ± 20	25 ± 3	...	...	6.239 ± 1.754	...	...
J2311+4543	A	1	135 ± 22	128 ± 15	14 ± 2	...	...	28.796 ± 6.801	3.91	10.5
J2311+4543	A	2	28 ± 10	28 ± 7	<21	93 ± 3	-159.8 ± 1.7	>2.626	...	...
J2311+4543	A	3	21 ± 10	11 ± 5	49 ± 21	758 ± 11	135.0 ± 0.8	0.347 ± 0.272	...	...
J2311+4543	A	4	77 ± 33	12 ± 5	393 ± 164	1214 ± 82	143.7 ± 3.9	0.020 ± 0.015	...	...
J2312+7241	C	1	131 ± 32	105 ± 20	27 ± 5	...	...	2.893 ± 1.048	3.15	3.93

**Table 7.** Model Fit Parameters *continued*

Source (J2000) (1)	Obs (2)	Comp (3)	$S_{\text{tot}}$ (4)	$S_{\text{peak}}$ (5)	$d$ (6)	$r$ (7)	$\theta$ (8)	$T_b$ (9)	$T_{b,\text{min}}$ (10)	$T_{b,\text{lim}}$ (11)
J2322+4445	A	1	$129 \pm 27$	$122 \pm 18$	$12 \pm 2$	...	...	$32.019 \pm 9.516$	3.99	10.6
J2322+4445	A	2	$21 \pm 11$	$25 \pm 9$	$<30$	$107 \pm 5$	$15.0 \pm 2.7$	$>0.906$	...	...
J2322+5057	A	1	$155 \pm 31$	$139 \pm 21$	$19 \pm 3$	...	...	$16.584 \pm 4.829$	3.84	10
J2322+5057	A	2	$52 \pm 23$	$20 \pm 8$	$69 \pm 29$	$86 \pm 14$	$170.9 \pm 9.4$	$0.414 \pm 0.305$	...	...
J2322+5057	A	3	$41 \pm 17$	$29 \pm 10$	$39 \pm 13$	$194 \pm 7$	$-150.4 \pm 2.0$	$0.994 \pm 0.633$	...	...
J2322+5057	A	4	$56 \pm 22$	$27 \pm 10$	$60 \pm 21$	$253 \pm 11$	$-116.3 \pm 2.4$	$0.589 \pm 0.375$	...	...
J2322+5057	A	5	$20 \pm 12$	$19 \pm 8$	$<31$	$477 \pm 7$	$-132.3 \pm 0.8$	$>0.767$	...	...
J2322+5057	A	6	$39 \pm 19$	$17 \pm 8$	$64 \pm 29$	$736 \pm 15$	$-118.7 \pm 1.1$	$0.360 \pm 0.295$	...	...
J2330+3348	C	1	$142 \pm 39$	$133 \pm 27$	$21 \pm 4$	...	...	$14.479 \pm 5.772$	4.55	5.72
J2354+4553	A	1	$122 \pm 29$	$122 \pm 20$	$<14$	...	...	$>29.156$	3.98	10.7

**Columns:** (1) – IAU Source name(J2000); (2) – observing epochs – A: October 2010; B: May 2011 and C: October 2011; (3) – I.D. number of Gaussian model fit component; (4) – total flux density of the component [mJy]; (5) – peak flux density of the component [mJy/beam]; (6) – component size [ $\mu\text{as}$ ], with upper limits shown in italics; (7) – component’s offset from the core [ $\mu\text{as}$ ]; (8) – position angle of the offset [degrees]; (9) – brightness temperature obtained from the model fits [ $\times 10^{10}$  K], with lower limits shown in italics; (10) – visibility based estimate of the minimum brightness temperature [ $\times 10^{10}$  K]; (11) – visibility based estimate of the maximum resolved brightness temperature [ $\times 10^{10}$  K].  
 (This table is also available in a machine-readable and Virtual Observatory (VO) forms in the online journal.)